Catena 267 (2026) 109971

Contents lists available at ScienceDirect

Catena

journal homepage: www.elsevier.com/locate/catena

Cosmogenic nuclide ^{26}Al—^{10}Be disequilibrium used to quantify Quaternary loess cover and integrated bedrock denudation rates in the Western Mecsek Mountains, Pannonian Basin

Zsófia Ruszkiczay-Rüdiger [a,b,*], Mads Farschou Knudsen [c], Márton Bauer [d], Tamás Telbisz [e], ASTER Team [f], Krisztina Sebe [g]

[a] Institute for Geological and Geochemical Research, HUN-REN Research Centre for Astronomy and Earth Sciences, Hungary
[b] HUN-REN CSFK, MTA Centre of Excellence, Hungary
[c] Department of Geoscience, Aarhus University, Denmark
[d] Authority for the Supervision of Regulated Activities, Hungary
[e] Eötvös University, Institute of Geography and Geology, Department of Physical Geography, Hungary
[f] Aix-Marseille Univ., CEREGE, France; Georges Aumaître, Karim Keddadouche
[g] HUN-REN–MTM–ELTE Paleontological Research Group, Hungary

ARTICLE INFO

Keywords:
Paired ^{26}Al/^{10}Be denudation rate
Cosmogenic disequilibrium
Loess cover
Quaternary
Monte Carlo modelling

ABSTRACT

This study aims to quantify bedrock denudation rates of ridge tops and small catchments in the Western Mecsek Mts, a low-elevation hilly area currently being exhumed from under its Quaternary loess cover. Low ^{26}Al/^{10}Be ratios indicate unsteadiness caused by significant past burial of the bedrock surfaces. A Monte Carlo model was developed to determine the true rate of bedrock denudation by revealing and considering the temporal evolution of the loess cover as a function of glacial-interglacial climate. In case the most common single nuclide ^{10}Be approach was used, the true lowering rate of bedrock would have been overestimated by a factor that increases with the shielding time. The modelled integrated bedrock denudation rates were between 5 ± 5 m/Ma and 19 ± 8 m/Ma depending on the duration of the loess cover. They were similar for the ridge crests and basin-averaged samples suggesting a steady relief during the last 1 Ma. Our results suggest that the high risk radioactive waste disposal planned to be implemented in the study area is safe in terms of denudation: it is not threatened by exhumation in a million years timescale. Our study demonstrates that the use of a paired ^{26}Al/^{10}Be approach is recommended to avoid overestimation of the true bedrock denudation by testing the presumption of cosmogenic nuclide equilibrium. This is true not only for large catchments and formerly glaciated areas, but also in settings where past sediment cover may have lasted long enough to lower the CRN ratio.

1. Introduction

The study of long-term landscape evolution was revolutionised over the last decades by the use of cosmogenic radionuclide (CRN) ^{10}Be concentrations in detrital quartz and in quartz-containing bedrock surfaces for the direct quantification of catchment-wide (CW) and local denudation rates. The first applications appeared by the end of the 20th century (Nishiizumi et al., 1986; Lal, 1991; Bierman and Steig, 1996; Granger et al., 1996) and were followed by an exponentially increasing number of related studies from the beginning of the 21St century (Granger and Riebe, 2014; Codilean et al., 2018, 2022). During this time, ^{10}Be was the "working horse" used to determine both local and CW denudation rates in a wide range of climatic, topographic and tectonic settings (Bierman et al., 2004; Portenga and Bierman, 2011; Granger and Schaller, 2014).

The most common, single-nuclide approach assumes that ^{10}Be concentrations have reached steady-state and thus does not enable to decipher complex geomorphic processes that may affect CRN concentrations. Disequilibrium between CRN concentrations can be revealed by the use of two CRNs with different half-lives, such as the ^{26}Al—^{10}Be pair. The effect of CRN disequilibrium on denudation rates was already discussed in early studies on slowly eroding landscapes (Bierman and Turner, 1995; Small et al., 1997). However, the use of several CRNs for the determination of surface denudation rates was limited, as they were

* Corresponding author.
E-mail address: rrzsofi@geochem.hu (Z. Ruszkiczay-Rüdiger).

https://doi.org/10.1016/j.catena.2026.109971
Received 5 September 2025; Received in revised form 25 February 2026; Accepted 28 February 2026
Available online 9 March 2026

mostly applied to decipher glacial landscape evolution processes, like quantification of CRN inheritance from previous glacial phases and glacial erosion rates at different geomorphological domains of the former ice sheets (Corbett et al., 2013; Strunk et al., 2017; Andersen et al., 2018). Others estimated the time spent ice covered and ice free during the Quaternary glaciations (Stroeven et al., 2002; Knudsen et al., 2015; Knudsen and Egholm, 2018; Young et al., 2021; Walcott-George et al., 2025) or highlighted the shielding effect of ice cover in decreased CRN ratio CW samples (Jautzy et al., 2024). The recent review of Halsted et al. (2025) discussed the importance of the paired nuclide approach for the determination of erosion rates where burial during transport can be revealed by higher ^{26}Al denudation rates compared to ^{10}Be values. Jautzy et al. (2024) showed considerable CRN unsteadiness in formerly glaciated landscapes by comparing CW denudation rates in formerly glaciated and unglaciated parts of the Vosges Mountains using the paired ^{26}Al—^{10}Be approach. They found a clear link between low ^{26}Al/^{10}Be ratios and former long-lasting and repetitive ice shielding of the studied catchments.

During the Quaternary glaciations the low elevation mid-latitude areas to the south of the Fennoscandian Ice Sheet were in the periglacial zone characterized by tundra and grassy-steppe vegetation with mass deposition of eolian dust (Haase et al., 2007; Obreht et al., 2019; Ludwig et al., 2021). Accordingly, CRN denudation rates of these regions are not affected by former ice covers. However, widespread occurrence of loess-paleosoil sequences in up to several tens of meters thickness is typical in this zone. The current cessation of eolian dust deposition together with hiatuses in the loess profiles indicate that the warmer and more humid interglacials were not favourable for loess deposition and were characterized rather by surface denudation and/or paleosoil formation (Marković et al., 2015; Sümegi et al., 2018, 2019). During the periods of loess cover, the bedrock erosion ceases and the surface is shielded from cosmic irradiation. Therefore, loess has a considerable effect on CRN concentrations in bedrock and therefore also on the estimated single nuclide CRN denudation rates used to quantify how the landscape has changed through time. This invokes the need for the application of the paired ^{26}Al—^{10}Be approach to acquire realistic long term surface denudation rates.

This study aims at investigating denudation rate in the Western Mecsek Mountains. We use denudation rate to express the total surface lowering rate and sometimes erosion rate is used as a synonym. The research question was risen to take care of the safety requirements of the high activity radioactive waste disposal site planned to be implemented in the study area. According to the Section 11 (1) (b) of the Decree [9] of the Ministry of Industry, Trade and Tourism of Hungary, a repository may be sited only where the degree of geodynamic stability of the geological environment is considered, and the safety assessment can be demonstrated. According to point 3 of Annex 3 to the Decree, the site's geodynamic stability, including the safe subsurface depth shall be assessed on a geological timescale of at least 10 kyrs (Kovács, 2004). In the study area the nuclear waste disposal facility is planned to be implemented in a subsurface depth of 500–1000 m, in the surroundings of the village of Boda (Nős, 2020). In study area the estimation of the bedrock denudation rate is challenged by the presence of loess cover. Shielding effect of the loess may have a considerable effect on the apparent denudation history of the underlying bedrock surface and may provide a possible explanation on the discrepancies of single nuclide surface denudation rates and those determined by other approaches like sediment gauging, as reported by previous studies in diverse geological settings (Meyer et al., 2010a; Schaller et al., 2001, 2016, 2025). Our study area, the Mecsek Mountains meets all requirements for such an investigation: it is i) a non-glaciated hilly landscape, ii) partially covered by loess with variable thickness and a stratigraphic record documenting repeated phases of loess accumulation and erosion (Sebe et al., 2025), iii) homogeneous siliciclastic basement suitable for the application of the ^{26}Al—^{10}Be CRN pair. The main objective of our study is to quantify the bedrock denudation rate over the last 1 Ma considering the shielding effect of the intermittent loess cover using a Monte Carlo (MC) inversion modelling approach developed by Knudsen et al. (2015). Within this framework, the percentage of time spent under a loess cover is modelled together with the bedrock denudation rate during periods of exposure. This is the first study addressing the shielding effect of a loess cover and it allows estimation of the time-integrated bedrock denudation rate relevant over the last 1 Ma.

2. The study area

2.1. Location, geology and climate

The Mecsek Mountains are located in the southern part of the Pannonian Basin (46.1°N; 18.1°E) (Fig. 1). Our study is focussing on its western part (Western Mecsek; WM) dominated by a Cretaceous anticline structure situated to the north of a major Neogene strike-slip zone, the Mecsekalja Dislocation Zone (Sebe et al., 2008). The hinge of the anticline has been eroded and a main east-west trending topographic ridge has developed on erosion resistant Lower Triassic sandstones and conglomerates on its northern limb (Figs. 1 and 2). To the south of the main ridge, Permian to Triassic siliciclastic sediments have subsequently been exposed in the core of the anticline. This is the planned location of the high-level radioactive waste disposal facility (Nős, 2020). During the Late Miocene, the study area was surrounded and partly covered by the sediments of Lake Pannon (Sebe and Konrád, 2013). Development of the present-day drainage network started after the disappearance of Lake Pannon ~6.5 Ma ago (Magyar et al., 1999). After the Late Miocene, the area was subject to tectonic movements due to the ongoing strike slip faulting, moderate uplift and surface denudation (Sebe et al., 2008). The Upper Miocene sediments were eroded from the study area; only few patches in up to 3 m thickness have been preserved in geomorphologically favourable conditions (Sebe and Konrád, 2013).

The elevation of its hilly landscape is ~100–600 m asl. with a humid continental temperate climate (mean annual temperature of 9–11 °C, mean annual precipitation: 500–750 mm; Kottek et al., 2006; Mersich et al., 2001). Under the current interglacial conditions, the area is covered by deciduous forests where fluvial erosion-sedimentation and soil formation are the main landscape forming processes. During glacials, while the surrounding mountains of the Alps and Carpathians were glaciated, the interior of the Pannonian Basin remained ice-free (Ehlers and Gibbard, 2004). It was a landscape dominated by periglacial activity, with discontinuous to sporadic permafrost, where the climate was cold and dry with a mean annual air temperature of 0 ± 2 °C and a mean

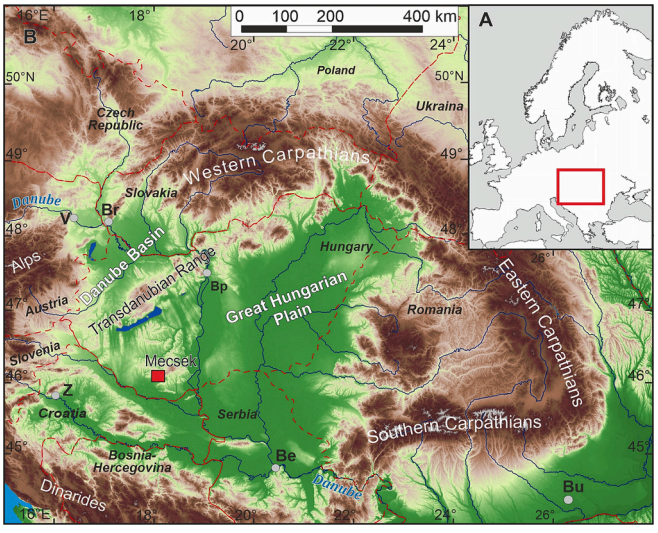

Fig. 1. Location of the study area in Europe (A) and in the Pannonian Basin (B). Be: Beograd, Bp: Budapest, Br: Bratislava, V: Vienna, Z: Zagreb.

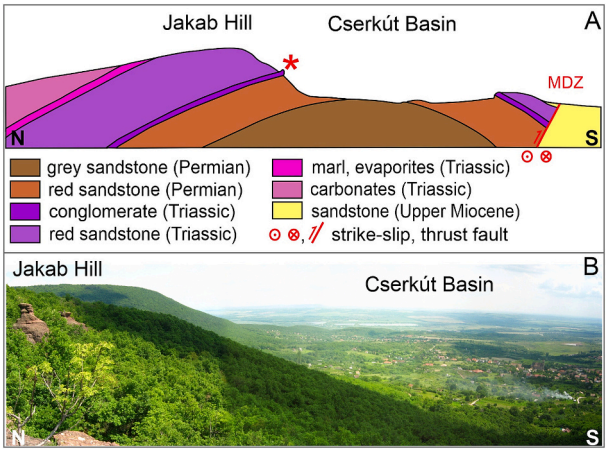

Fig. 2. A: Geological cross-section (not to scale) (A) and photo (B) of the eastern part of the Western Mecsek Anticline. The photo was taken from the location of the M15 sample (Fig. 4). The red star indicates the outcropping base conglomerates of the Triassic succession, appearing on the left of the photo of inset B. MDZ: Mecsekalja Dislocation Zone. Location of the profile is shown on Figs. 4 and 5A. (For interpretation of the references to colour in this figure legend, the reader is referred to the web version of this article.)

annual precipitation of 300–500 mm (Ruszkiczay-Rüdiger and Kern, 2016). During this time the forests were replaced by cold continental steppe and tundra-like vegetation (Pazonyi, 2004; Sümegi et al., 2013; Feurdean et al., 2014). These environmental conditions favoured an eolian landscape evolution dominated by wind erosion and deflation (Sebe et al., 2011; Ruszkiczay-Rüdiger et al., 2011) and eolian dust deposition, which led to accumulation of thick loess sequences in low-elevation hilly areas (Horváth and Bradák, 2014; Marković et al., 2015; Lehmkuhl et al., 2021; Ludwig et al., 2021), including the WM (Sebe et al., 2025).

2.2. Cover sediments and Pliocene-Pleistocene landscape evolution

After the disappearance of the Lake Pannon, the study area was subject to surface denudation and/or terrestrial red clay formation. The Tengelic Red Clay Formation (TRC) developed either on bedrock or on Upper Miocene sediments with an assigned age of ~3.5–1 Ma in a variable thickness between zero and ~ 30 m. It is built up of red, reddish yellow or variegated clay, clayey silt, and pedogenic carbonate lenses, beds and concretions. Sand is also present in varying amounts. It formed under a Mediterranean climate and consists of palaeosols, the in situ weathering residue of the underlying rocks, and their material redeposited by surface runoff, with additions of airborne dust (Kovács et al., 2011; Csillag et al., 2023). After 1 Ma, the climate deterioration led to the cessation of in situ clay formation, which was replaced by the accumulation of eolian dust during glacials and soil formation and/or denudation during interglacials. The resulting loess deposits also have large spatial variability in the Western Pannonian Basin, with a thickness changing from zero to 97 m. Several hiatuses and paleosoil horizons within the ~1 Ma to 0.02 Ma old sediment sequence mark longer repeated periods with and without dust deposition and surface denudation (Koloszár and Marsi, 2010; Marković et al., 2011; Horváth and Bradák, 2014; Sümegi et al., 2018; Thiel et al., 2014; Újvári et al., 2014a, 2014b; Novothny et al., 2020, 2023).

In the WM, the Permian-Triassic basement rocks are usually directly overlain by a discontinuous loess cover up to 400–500 m asl elevation, suggesting that most of the TRC was eroded before the onset of loess deposition. Remnants of the TRC were preserved under the loess only in the westernmost area in some local depressions and paleokarst features up to a few meters thickness (Sebe et al., 2025), but it could have been more extended in the Pliocene and early Quaternary. The preserved loess-paleosoil formations of the WM are incomplete and rarely exceed 15 m thickness. Currently, the loess cover is missing from the highest ridges and is thickening towards the lower areas in the southern and western part the study area (Sebe et al., 2025).

3. Methods and sampling strategy

3.1. Determination of cosmogenic nuclide surface denudation rates

Determination of the ^{10}Be and ^{26}Al CRN abundances in stream sediments is suitable for the estimation of local and CW denudation rates, while in exposed bedrock and regolith surfaces of steadily eroding ridges and hilltops they enable the estimation of local denudation rates. CRN are produced and accumulate in situ in the uppermost few meters of the lithosphere. Their production rates decrease exponentially with depth in rock or soil. In case of an eroding surface, the uppermost rock layers are removed and transported by the rivers and new rock layers become exposed to cosmic rays in the uppermost zone (Bierman and Steig, 1996; Bierman et al., 2002). Accordingly, CRN concentrations in both surface rock layers and stream sediments integrate the history of a grain's approach towards the surface and it can therefore be used to calculate the denudation rate. The simple denudation rate typically integrates over 10^3 to 10^5 years timescales in landscapes of fast and slow denudation, respectively (Bierman et al., 2004; Granger and Riebe, 2014; Granger and Schaller, 2014).

If the bedrock was shielded by an intermittent loess cover for considerable time during the Quaternary, it must have affected the CRN concentrations of the bedrock, and thus the estimated denudation rates. Temporal shielding decreases CRN production, leading to a transient signal characterized by lower CRN concentrations and a decreased ^{26}Al/^{10}Be ratio compared to the surface production rate expected for rocks of constant exposure, similarly to locations affected by former glaciation (Corbett et al., 2013; Knudsen et al., 2015; Andersen et al., 2018; Jautzy et al., 2024). As a consequence, the apparent denudation rates are overestimated and are inconsistent for the two nuclides, with faster rates for the shorter-lived ^{26}Al. Besides, the bedrock surface is not eroded when covered by loess, which means that the time-integrated denudation rate for the last 1 Ma must be lower compared to the uncovered (Holocene, interglacial) denudation rates targeted by the measurement of CRN concentrations of currently uncovered rocks and stream sediments.

In this study, we develop a new method that is applied to samples from the WM area to estimate both the recent and long-term denudation rates of the basement rocks. This is possible through quantification of the effect of the loess cover achieved by modelling the evolution of the concentrations of the ^{26}Al—^{10}Be CRN pair using a modified version of model approach presented in Knudsen et al. (2015).

3.2. CRN sampling and laboratory procedures

Samples were collected during two field campaigns. In 2016 both local (n = 10) and CW (n = 6) samples were collected on the hilltop ridges and on southern and western sides and of the WM (M01 to M16) (Fig. 3). In 2019, additional sampling of stream sediments for CW denudation rates occurred on the northern limb of the WM anticline (n = 4; ACH, GUB, SPI, VAD), where the Triassic sandstones are transported towards sinkholes developed on Triassic limestones (Fig. 4).

All local samples were collected on flat ridge tops and hilltop surfaces of Permian and Triassic sandstone or conglomerate. The samples were coming either from uncovered bedrock (n = 3) or from bedrock fragments in the regolith (n = 4) and also from well-mixed regolith/soil (n = 3) (Table 1, Supplementary Table S1; Fig. 3). The thickness of the well-mixed soil is usually around 10–15 cm. For soil samples taken from the well-mixed layer (M01, M08, M10), the CRN concentrations are assumed to be constant throughout the well-mixed layer and no correction for self-shielding is applied (Granger and Riebe, 2014). If the

Fig. 3. Photos of some typical sample locations. A-C: stream sediment sample sites; D-G: regolith samples form gentle ridge tops and hilltop surfaces; H-I: bedrock samples from uncovered rock surfaces.

sample was a piece, or several pieces, from the weathered bedrock within the regolith matrix, we corrected for its thickness and subsurface depth (M09, M10, M12, M16).

Samples of the 2016 campaign were processed at the Cosmogenic Nuclide Sample Preparation Laboratory of the Institute for Geological and Geochemical Research (Budapest, Hungary; https://www.geochem.hu/facilities/lab_en.html). Samples were crushed and sieved to a grain size of 0.25–0.5 mm. The samples were treated by 10% H_2O_2 at 60 °C for 1–2 days to get rid of their organic matter content. As the red matrix of the sandstones and conglomerates contained large amount of iron, their iron content was removed using the Na-dithionite-citrate method (Mehra and Jackson, 1960). The quartz concentration of the samples was first increased via density separation using heavy liquids (LST Fastfloat).

Chemical sample processing followed the procedures of Brown et al. (1991); Merchel and Herpers (1999) and Merchel et al. (2019), as described by Ruszkiczay-Rüdiger et al. (2021). For samples M10, M11 and M16, some solid precipitate was observed during sample evaporation. These were most probably Al-fluorides, which can lead to some loss of Al, and thus to biased $^{26}Al/^{27}Al$ ratios and eventually to erroneously low ^{26}Al concentrations (Ruszkiczay-Rüdiger et al., 2021). The precipitates could not be broken and despite the potential problems they may cause (at that time not yet fully tested), the processing of these samples was continued with the rest of the sample set. Purified BeO was mixed with Nb powder and Al_2O_3 was mixed with Ag powder and targets were prepared for AMS (Accelerator Mass Spectrometry) measurement

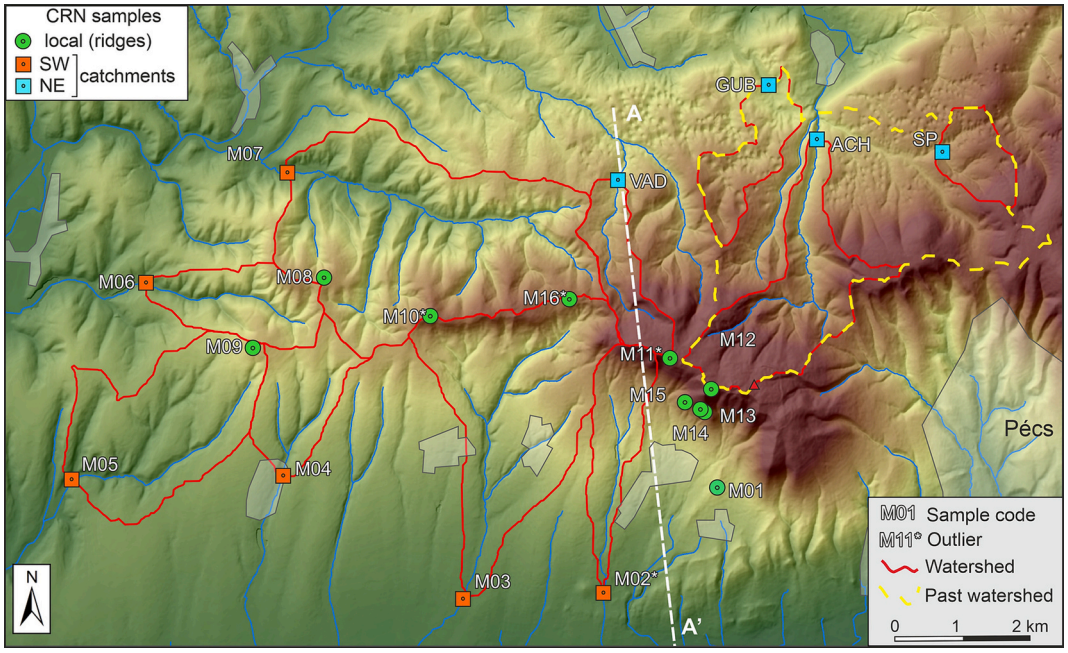

Fig. 4. Topography of the study area with sample locations and drainage basins. A-A' is the location of the profile on Fig. 2A. Yellow dashed line is the reconstructed former catchment of the GUB sample, before a past river piracy that cut its major, eastern part with quartz containing lithologies (Fig. 5A). (For interpretation of the references to colour in this figure legend, the reader is referred to the web version of this article.)

Table 1
Selected field data and laboratory measurement results. For more data, please refer to Supplementary Tables S1, S2, S3 and S4. L: local sample; SW: catchment-wide sample from the southwestern region; NE: catchment-wide sample from the northeastern region.

Sample	Latitude	Longitude	Elevation	Sample type		Location	^{10}Be	1σ ^{10}Be	^{26}Al	1σ ^{26}Al	^{26}Al/^{10}Be	1σ ^{26}Al/^{10}Be
	N (°)	E (°)	(m, asl)				(at/g$_{qtz}$)	(at/g$_{qtz}$)	(at/g$_{qtz}$)	(at/g$_{qtz}$)		
M01	46.0809	18.1355	298	regolith	L	flat top ridge	138,462	7809	657,972	53,856	4.75	0.47
M02	46.0667	18.1140	164	sand	SW	stream sediment	39,621	3043	224,089	23,342	5.66	0.73
M03	46.0657	18.0872	159	sand	SW	stream sediment	92,226	4916	455,373	42,341	4.94	0.53
M04	46.0818	18.0523	184	sand	SW	stream sediment	116,753	6213	532,948	41,349	4.56	0.43
M05	46.0809	18.0120	144	sand	SW	stream sediment	163,036	7010	722,355	52,281	4.43	0.37
M06	46.1073	18.0257	172	sand	SW	stream sediment	98,327	6002	456,372	40,220	4.64	0.50
M07	46.1220	18.0526	173	sand	SW	stream sediment	112,326	5183	592,074	47,152	5.27	0.49
M08	46.1083	18.0598	359	regolith	L	hilltop	177,312	10,768	747,888	51,912	4.22	0.39
M09	46.0988	18.0464	331	regolith	L	flat top ridge	171,308	6937	1,009,623	58,787	5.89	0.42
M10	46.1032	18.0802	430	regolith	L	hilltop	119,744	6095	491,975	39,168	4.11	0.39
M11	46.0981	18.1263	573	regolith	L	hilltop	149,165	6781	436,581	38,688	2.93	0.29
M12	46.0941	18.1341	579	regolith	L	hilltop	121,039	9290	820,597	67,309	6.78	0.76
M13	46.0912	18.1327	444	bedrock	L	rock formation	98,237	8749	479,245	51,746	4.88	0.68
M14	46.0913	18.1322	442	bedrock	L	rock formation	124,758	5855	633,274	55,537	5.08	0.50
M15	46.0922	18.1292	425	bedrock	L	rock formation	146,702	13,224	831,233	75,892	5.67	0.73
M16	46.1059	18.1069	409	regolith	L	hilltop	159,660	7285	519,328	49,980	3.25	0.35
ACH	46.1278	18.1538	270	sand	NE	stream sediment	243,536	7575	1484 803	83,099	6.10	0.39
GUB	46.1348	18.1446	261	sand	NE	stream sediment	217,352	7070	1,331,550	70,967	6.13	0.38
SP	46.1260	18.1780	349	sand	NE	stream sediment	144,162	5376	825,272	53,728	5.72	0.43
VAD	46.1215	18.1158	287	sand	NE	stream sediment	131,149	4371	737,651	54,151	5.62	0.45

of their ^{10}Be/^{9}Be ratios at ASTER, the French national AMS facility located at CEREGE, Aix en Provence (Arnold et al., 2010).

At ASTER, beryllium measurements were calibrated against the ASTER in-house STD-11 standard (^{10}Be/^{9}Be = (1.191 ± 0.013) × 10^{-11}, equivalent to NIST_27900 (Braucher et al., 2015), considering the ^{10}Be half-life of (1.387 ± 0.012) × 10^{6} years (Chmeleff et al., 2010; Korschinek et al., 2010)). The ^{26}Al measurements were normalised to the standard SM-Al-11 with a ^{26}Al/^{27}Al ratio of (7.401 ± 0.064) × 10^{-12}, a secondary standard material directly traceable to primary standards (Arnold et al., 2010; Merchel and Bremser, 2004; Rugel et al., 2016) considering a ^{26}Al half-life of (705 ± 17) × 10^{3} years (Nishiizumi, 2004). Stable ^{27}Al content of the samples was determined using Inductively Coupled Plasma-Optical Emission Spectrometry (ICP-OES; at CEREGE, Aix en Provence, France). Analytical uncertainties (reported as 1σ) include uncertainties concerning sample weighing, AMS counting statistics, ^{10}Be/^{9}Be and ^{26}Al/^{27}Al ratios of the standards and chemical blank measurements and for ^{10}Be an external AMS error of 0.5% (Arnold et al., 2010) and a 3% stable ^{27}Al measurement uncertainty.

The 2019 sample batch was processed at the Cosmogenic Nuclide Laboratory of the University of Edinburgh. The crushed samples were sieved to obtain the 250–710 μm fraction. Quartz was isolated through repeated acid etching following standard procedures (Nishiizumi et al., 2007; Bierman et al., 2002). ^{10}Be and ^{26}Al was selectively extracted from 21 to 25 g of the pure quartz following standard methods (Bierman et al., 2002; Kohl and Nishiizumi, 1992). Process blanks (n = 2) were spiked with 250 mg ^{9}Be carrier (Scharlau Batch# 10843401) and 1.5 g ^{27}Al

carrier (SpexCertiPrep, Batch# CL10–124ALY). Samples were spiked with 250 mg ^{9}Be carrier and up to 1.5 g ^{27}Al carrier.

The AMS cathodes prepared at Edinburgh University were measured on the 5MV Pelletron accelerator mass spectrometry system at the SUERC AMS Laboratory (Freeman et al., 2007; Xu et al., 2015). ^{10}Be/^{9}Be measurements were normalised to the NIST SRM-4325 Be standard material with a revised (Nishiizumi et al., 2007) nominal ^{10}Be/^{9}Be of 2.79×10^{-11}. ^{26}Al/^{27}Al measurements were normalised to the Purdue Z92–0222 Al standard material with a nominal ^{26}Al/^{27}Al of 4.11×10^{-11}, which agrees with the Al standard material of Nishiizumi (2004). The SUERC ^{10}Be-AMS is insensitive to ^{10}B interference (Xu et al., 2013) and the interferences with ^{26}Al detection are well characterized (Xu et al., 2014). AMS machine blanks were 2.18 ± 0.48E-15 and 0.99 ± 0.7E-15 for ^{10}Be/^{9}Be and ^{26}Al/^{27}Al, respectively. Nuclide concentrations have been corrected for process blanks; uncertainties include propagated AMS sample/lab-blank uncertainty, a 2% ^{9}Be carrier mass uncertainty and a 3% stable ^{27}Al measurement (ICP-OES) uncertainty.

3.3. Delineation of watersheds for catchment-wide denudation rate calculations

The uncovered quartz-containing lithologies represent potential sources of the sampled sand in the creeks. The watersheds were outlined using a digital elevation model (DEM) digitized from 1:10000 topographic maps (Fig. 4). A 1:25000 geological map (Chikán and Chikánné, 1984) was used to constrain the geology of the study area (Fig. 5). The drainage basins are composed mostly of quartz-bearing Permian and Triassic sandstones and conglomerates, which are the source of the sampled river sediments (Figs. 3, 5A). Other parts of the catchments are on older Permian claystones or Triassic evaporites and carbonates. These areas do not yield quartz to the river load and these areas were therefore subtracted from the total area of the catchments. The mean elevation and coordinates of the above constrained catchment areas were extracted from the DEM and were used for calculation of the CW denudation rates. The present catchment of the GUB sample does not include areas of non-carbonate lithology (Figs. 4, 5, red contour), however its former catchment was reconstructed to be much larger (Figs. 4, 5, yellow dashed contour) that was cut by stream piracy. For the modelling the parameters of this larger catchment, so called GUB-Paleo were used (Supplementary Table S1).

The loess coverage also influences the extent of the sediment source area (Fig. 5B). However, its presence has been variable in time and space during the last 1 Ma, therefore its present day extent was not considered to reduce the area of sediment source as the uncertainty would be larger than its effect on the estimated denudation rates. The grain size used for the analysis was larger than the loess fraction, which assures that quartz coming from the Permian-Triassic bedrock was the exclusive source of the measured CRN concentrations.

3.4. Monte Carlo (MC) simulations of cosmogenic ^{10}Be and ^{26}Al concentrations

3.4.1. Geological parameters defining the model setup

The shielding effect of the intermittent loess cover reduces the CRN production rate in the rocks, biasing the apparent denudation rates if it is not accounted for. Therefore, the temporal evolution of the loess cover is modelled in order to achieve a valid quantification of the amount and rate of bedrock denudation.

During the Late Pliocene and Early Pleistocene, before the onset of loess formation, the bedrock could either be uncovered and subject to denudation or covered by a red clay formation (TRC, see section 2.2.; Kovács et al., 2011; Csillag et al., 2023). The oldest loess in the Pannonian Basin (dated to ~1 Ma, Koloszár and Marsi, 2010; Sümegi et al., 2018, 2019) constrained the timeframe of the model to the last 1 Ma. Loess formation ceased just before the Holocene interglacial (~11 ka; Újvári et al., 2016; Novothny et al., 2020, 2023), thus no upper time constraint was used. Based on the current, thickness of the loess in the study area (up to 15 m; Sebe et al., 2025) the mean loess thickness is allowed to vary between 3 and 20 m in the model. Loess is mostly deposited directly on bedrock and in lower areas it is deposited on red clay (TRC) or on Miocene sediments (Fig. 5A,B). Due to the possible presence of the TRC before the onset of loess deposition, for the 2.6 to 1 Ma period two slightly different model scenarios were used. Our Model A is simulating the scenario of uncovered bedrock exposed to cosmic irradiation and surface denudation before the onset of loess deposition at 1 Ma. For the samples that Model A could not find a geologically reasonable model fit to the measured CRN data, a different scenario was applied: Model B accounts for a few meters of TRC cover between the onset of the Quaternary and 1 Ma, which partially shielded the bedrock and prevented it from eroding. Model A and B scenarios cover the period starting with the beginning of the Quaternary, as any earlier onset would not affect the narrative of the outcoming story. For the last 1 Ma the two models are identical.

3.4.2. Model setup

In our setup, we adopt the model approach by Knudsen et al. (2015). For the last 1 Ma this involves the basic assumption of that the exposure/burial history can be divided into two distinct regimes: (i) cold glacial intervals when bedrock is covered by loess and therefore partially shielded from cosmic irradiation and not affected by surface erosion, and (ii) warm interglacial intervals experiencing active subaerial erosion and full exposure, assuming no shielding for example by snow or vegetation. For each Monte Carlo simulation, the forward model randomly selects a set of parameters (δ^{18}O threshold, loess thickness, denudation rate) that together define the exposure and erosion history of a hypothetical sample. The model then integrates the ^{10}Be and ^{26}Al nuclide production through time as a function of the exposure history (with or without loess cover) and erosion history. The forward model considers the thickness of the loess when the surface is covered, and time-dependent changes in the sample depth defined by the erosion history. The forward model calculates the ^{10}Be and ^{26}Al concentrations of each hypothetical sample, and each simulation is then either accepted or rejected based on comparison with the measured concentrations using rejection sampling (Knudsen et al., 2015; Nørgaard et al., 2023). Using this probabilistic inverse model approach, it is possible to map out the most likely exposure and erosion history for each field sample based on their measured ^{10}Be and ^{26}Al concentrations.

To simulate the timing and duration of periods with and without loess cover we follow the approach used to define ice-covered and uncovered periods for samples in Greenland (Fig. 6; Knudsen et al., 2015; Strunk et al., 2017; Knudsen and Egholm, 2018). In our study area the loess covered periods are defined by this two stage model based on a δ^{18}O threshold value applied in the global benthic marine δ^{18}O record (Lisiecki and Raymo, 2005) (Fig. 6). The correlation between paleoclimatic records from the deep-sea floor and terrestrial records from loess units was already revealed by Kukla and Cílek (1996). Accordingly, the periods of loess deposition and its cessation can be approximated by the climate oscillations recorded in the marine δ^{18}O record. This way the simulations aimed at selecting a threshold δ^{18}O value to define the length and number of warm climate spells, when the bedrock was uncovered and exposed to cosmic rays and surface denudation. The δ^{18}O threshold is one of the free parameters in our model and it is allowed to vary between 3.2 ‰ and 4.7 ‰ in model A. The δ^{18}O threshold value is more restricted (3.2–4.0 ‰) for model B in order to get enough accepted model runs for the group of samples characterized by low ^{26}Al/^{10}Be ratios. (Table 2).

The time-integrated denudation rate over the last 1 Ma (integrated erosion rate, m/Ma) is calculated from the erosion history that depend on the δ^{18}O threshold value, the loess thickness, and the bedrock denudation rate during periods without loess cover (bedrock erosion rate; m/Ma). The average thickness of loess cover during cold periods was a variable between 3 m and 20 m during periods of loess cover and it

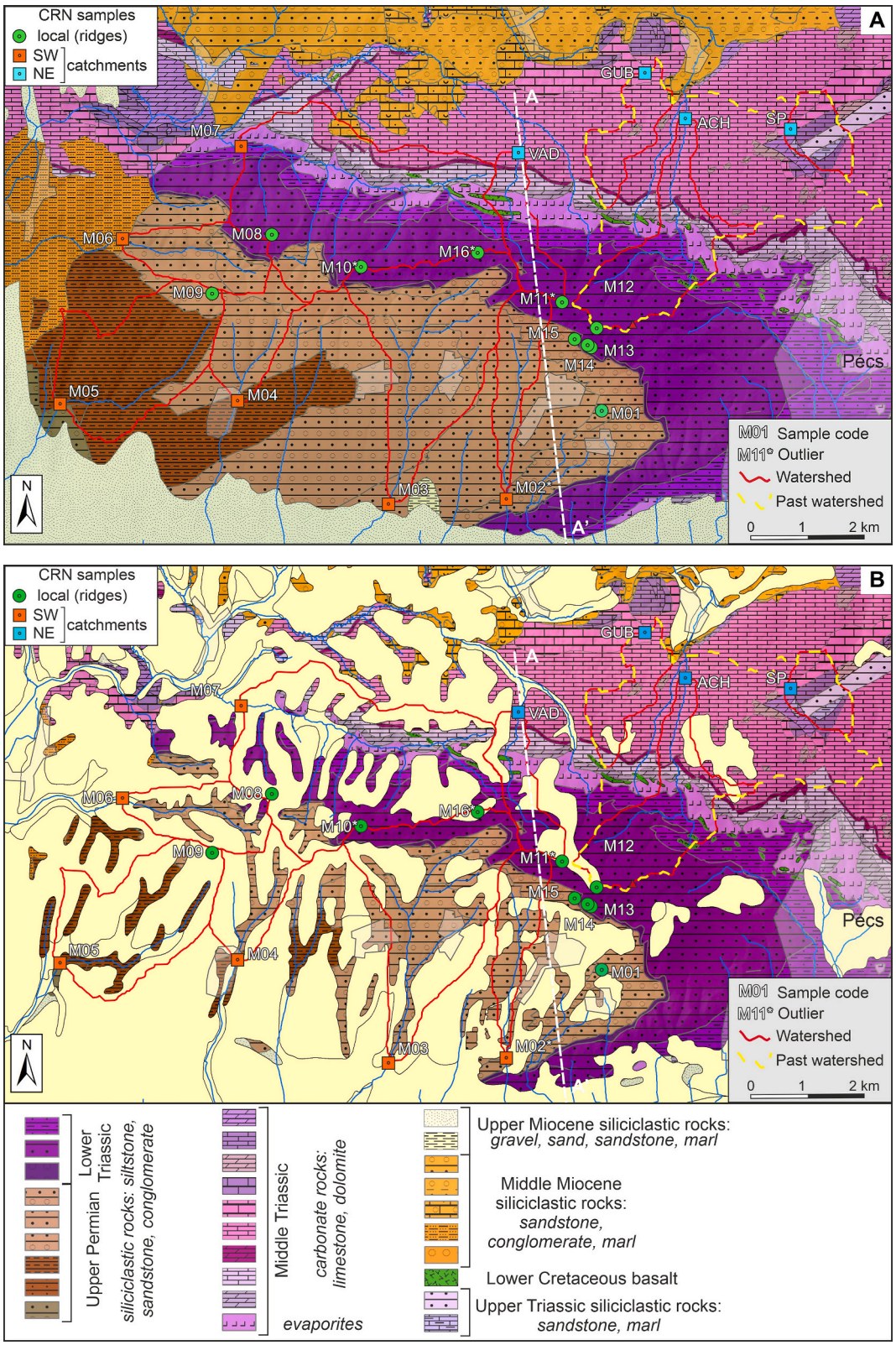

Fig. 5. Geological map of the study areas with sample locations and drainage basins. A: Uncovered geological map (Chikán and Chikánné, 1984. 1:25000). A-A' is the location of the profile on Fig. 2A. B: Geological map with estimated extent of present-day loess cover (based on geological map of Hungary 1:100000; Gyalog and Síkhegyi, 2005).

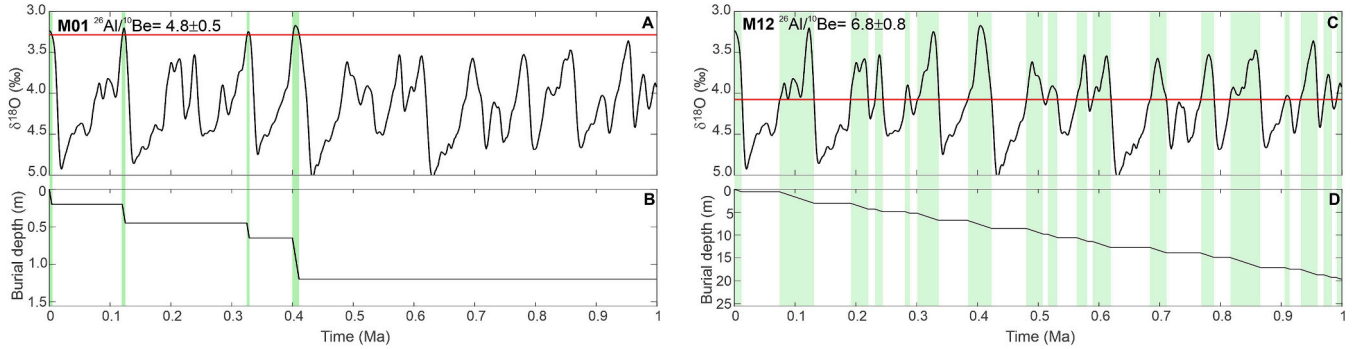

Fig. 6. The MC model to constrain the exposure-burial history. A and C: Timing and duration of the exposed and loess-covered periods as defined by a threshold value (red line) of the global benthic marine $\delta^{18}O$ record (Lisiecki and Raymo, 2005). B and D: burial history showing how the sample was exhumed due to bedrock erosion during the last 1 Ma. Burial depth mean burial under bedrock and does not include the loess cover. A and B show an example of a low $^{26}Al/^{10}Be$ ratio sample (M01), C and D show a high ratio sample (M12). Green shadows highlight periods of exposure and bedrock erosion. (For interpretation of the references to colour in this figure legend, the reader is referred to the web version of this article.)

Table 2
Variables and constants used for the calculation of simple denudation rates and MC modelling (qtz: quartz; SLHL: sea level high latitude).

Model parameter [unit]	Value	Reference
^{10}Be spallogenic production rate SLHL [atoms/g_{qtz}/yr]	4.01 ± 0.33	Borchers et al. (2016)
Scaling of muogenic production rates	Heisinger et al. (2002a, b) modified by Balco (2017), calculated using the code of Nørgaard et al. (2023)	
Attenuation lengths (neutrons, thermal muons, fast muons) [g/cm^2]	160, 1500, 4320	Heisinger et al. (2002a,b); Braucher et al. (2011)
Scaling of spallogenic production rates	time independent	Lal (1991)/ Stone (2000); calculated using Vermeesch (2007)
^{10}Be half-life [yr]	1,387,000 ± 12,000	Chmeleff et al. (2010); Korschinek et al. (2010);
^{26}Al half-life [yr]	705,000 ± 17,000	Nishiizumi (2004)
production rate ratio $^{26}Al/^{10}Be$	6.7 ± 0.6	Fenton et al. (2022)
Bedrock density [g/cm^3]	2.5	estimated value
Loess density [g/cm^3]	1.6	estimated value
Red clay density [g/cm^3]	2.0	estimated value
Number of simulations	100,000	
User defined bounds and the model parameters:		
Number of simulations	100,000	
Loess thickness during cold periods [m]	3–20	
Denudation rate when uncovered [m/Ma]	0.1–1000	
Model A	2.6–1 Ma: uncovered 1 Ma to present: intermittent loess cover	
Model B	2.6–1 Ma: covered by 3 m red clay 1 Ma to present: intermittent loess cover	
$\delta^{18}O$ threshold [‰]	Model A: 3.2–4.7 Model B: 3.2–4.0	

was zero for the time without loess cover. Using an average value for the loess-covered periods represents a simplification, but with the available data it would not be possible to resolve the detailed loess accumulation and denudation history, including thickness fluctuations within the loess covered periods.

The production and loss of ^{10}Be and ^{26}Al by decay and erosion were computed throughout the last 1 Ma using a wide range of combinations of the model parameters. The resulting CRN concentrations were compared to the measured values applying rejection sampling. The median of the accepted model parameters was treated as the most likely value and the associated uncertainty estimate is based on the 75% and 25% quartiles. The constants and variables along with the applied model parameters are described in Table 2.

The first model runs were designed to simulate fluctuations of the loess cover during the last 1 Ma, leaving the surface uncovered before this time (Model A). For the samples where the measured CRN concentrations could be reproduced Model A with a reasonably good fit, this scenario was used. However, for samples where Model A could not fit the measured CRN concentrations (no simulated concentrations within 1σ) because the measured $^{26}Al/^{10}Be$ ratio was too low, we used another model scenario (Model B). Model B is characterized by zero erosion and partial shielding by red clay (TRC) of the surface before the onset of loess deposition at 1 Ma. To keep the model simple, the thickness of this clay cover in Model B was constant for the entire timespan between 2.6 Ma and 1 Ma, and the minimum thickness needed to get a robust agreement with the measured CRN concentrations was searched in 1 m incremental steps.

4. Results

4.1. CRN measurement results

Results of the CRN measurements are presented in Table 1 and Supplementary Tables S2 and S3. The measured $^{10}Be/^{9}Be$ ratio of the samples varied between (6.74 ± 0.44)E-14 and (3.04 ± 0.18)E-13 for the 2016 sample batch and between (1.84 ± 0.06)E-13 to (3.19 ± 0.09) E-13 for the 2019 sample batch. The mean $^{10}Be/^{9}Be$ ratio of the process blanks was (6.34 ± 01.54)E-15 and (5.84 ± 1.18)E-15 for the 2016 and 2019 samples, respectively. The analytical uncertainties of the $^{10}Be/^{9}Be$ ratios had a mean of 5.6% and 3.8% for the 2016 and 2019 samples, respectively. The reported uncertainties include the ^{9}Be carrier concentration, weighing and the AMS measurements (including the process blanks) and standards' uncertainties.

For the 2016 batch, the natural Al content in rock was between 104 μg/g and 335 μg/g with a mean of 154 μg/g, and for the 2019 batch it was 244–359 μg/g averaging at 294 μg/g, thus no ^{27}Al carrier was added. The measured $^{26}Al/^{27}Al$ ratio varied between (8.50 ± 0.84)E-14 and (2.64 ± 0.16)E-13 and from (1.04 ± 0.06)E-13 to (2.45 ± 0.11)E-13 for the 2016 and 2019 samples, respectively. The mean $^{26}Al/^{27}Al$ ratio of the blanks of the 2016 batch was below the detection limit, therefore the sample ratios were corrected for the machine blank of (2.97 ± 1.21) E-15. For the 2019 batch, the mean $^{26}Al/^{27}Al$ blank ratio was (3.64 ± 2.34)E-15. The analytical uncertainties of the $^{26}Al/^{27}Al$ ratios of the samples had a mean of 7.9% and 5.5% for the 2016 and 2019 samples, respectively. The reported uncertainties of the ^{26}Al concentrations include ^{27}Al carrier concentration, weighing, measurement of the total ^{27}Al content (3%) and the analytical uncertainties of AMS measurements and standards including the process blanks.

^{10}Be concentrations were between (39.5 ± 3.0) kat/g_{SiO2} and (243.5

± 7.6) kat/g_{SiO2}. The ^{26}Al concentrations varied between (224.1 ± 23.3) kat/g_{SiO2} and (1484.8 ± 83.1) kat/g_{SiO2}. The lowest values for both nuclides belonged to the basin-wide sample M02. After sample collection it turned out that in the watershed of this sample (Kajdácsi creek) considerable amounts of mine waste from the former uranium mines had been piled up. This deep-mined debris being exposed to surface denudation must have diluted the natural CRN signal in the stream sediment. Accordingly, this sample was omitted from the modelling of surface denudation rates.

The ^{26}Al/^{10}Be ratios of the samples varied between 2.93 and 6.78. The samples with the lowest ratios (2.93–4.11) coincided with the those producing fluoride precipitates during sample processing (M10, M11, M16), suggesting that the low ratios are the consequence of the bias of the ^{26}Al concentrations due to the Al trapping effect of the fluoride precipitates (Ruszkiczay-Rüdiger et al., 2021). Therefore, these samples were also excluded from further discussion as analytical outliers.

The ^{26}Al/^{10}Be ratios of six samples agree within error with the surface production rate ratio of 6.7 ± 0.6 (Fenton et al., 2022), all the other samples remain below this value and plot well under the steady state erosion line on the exposure-burial diagram (Table 1, Supplementary table S4; Fig. 7). These lowered ^{26}Al/^{10}Be ratios indicate a transient CRN signal and complex exposure burial history, including considerable time spent (at least partially) shielded from cosmic rays (Lal, 1991).

4.2. Simple denudation rates

Simple ^{10}Be denudation rates vary between 19 ± 2 m/Ma and 45 ± 4 m/Ma. Simple ^{26}Al denudation rates were ~ 40% higher on average, varying between 21 ± 3 m/Ma and 64 ± 10 m/Ma (Table 3, Supplementary Table S4, Fig. 8). The divergent ^{10}Be and ^{26}Al denudation rates are indicative of a disequilibrium between the cosmogenic nuclide inventories, as also demonstrated by the low ^{26}Al/^{10}Be ratios of currently uncovered surface samples. These facts point to the existence of past shielding of the surface by loess. Considering the time needed to reach secular equilibrium (Lal, 1991; Integration time, T_{int}), these rates should be relevant for the last ~10–40 kyr with T_{int} between 17 ± 2 kyr and 40 ± k kyr for ^{10}Be and between 12 ± 1 kyr and 35 ± 2 kyr for ^{26}Al (Tables 3, S4). Except for the ^{26}Al integration times of the samples of fastest simple erosion rate, this period of time is longer than the time elapsed since the cessation of loess deposition, again suggesting that the nuclide inventories had not enough time to set the new equilibrium relevant to the current, interglacial/uncovered situation (Braucher et al., 2003).

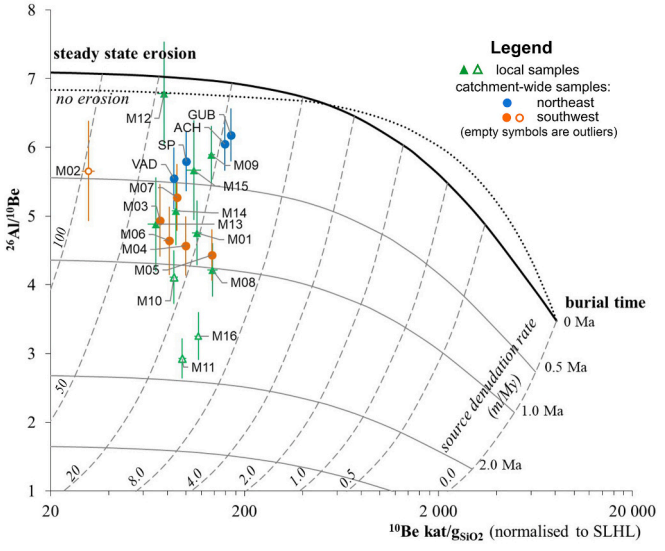

Fig. 7. Exposure-burial diagram of the samples. All but one samples perform apparent simple burial ages with values up to 1 Ma, suggesting transient CRN signal and complex exposure burial histories. Note that ^{10}Be uncertainties for the CW samples remain hidden because they are smaller than the size of the sample dots. For more explanations refer to section 4.1.

4.3. Exposure-burial history and denudation rates determined using MC simulations

4.3.1. The effect of model outcomes on surface cover before the onset of loess deposition

First, Model A was applied to all samples, which starts from an uncovered steadily eroded surface at 1 Ma. However, the concentrations simulated with Model A did not sufficiently overlap the measured concentrations for samples with a ^{26}Al/^{10}Be ratio below 5.4, suggesting that important aspects of the landscape evolution associated with these samples were not captured by this model (Fig. 9A). For these samples, we used Model B that is inspired by the stratigraphic record of the study area including remnants of a formerly more extended red clay cover (TRC, see section 2.2.) before the onset of loess formation at 1 Ma. By the introduction of this clay cover the simulated concentrations were in better agreement with the measured concentrations for the low ^{26}Al/^{10}Be ratio samples (Fig. 9B). The results of the MC modelling are presented in Table 3, Supplementary Table S5.

Model A worked well for the high-elevation northeastern catchments (ACH, GUB, SP, VAD) and for the sample coming from the highest hilltop (M12). Surprisingly, a sample from a lower flat ridge (M09) in the western, more covered part of the study area could also be modelled with Model A. All other samples from the lower, southern and western catchments as well as local hilltop and ridge samples could only be fitted with Model B (M01 to M08, M13, and M14). Applying Model B with a clay thickness of 1–2 m led to vastly improved model fits for these samples. However, they still required an almost full-time loess cover during the last 1 Ma (very low δ^{18}O threshold values) leading to unreasonably high bedrock denudation rates for the very short uncovered periods. For clay thicknesses of at least 3 m, the bedrock denudation rates decreased to values more like those published for similar climate and tectonic settings (e.g. Portenga and Bierman, 2011; see discussion in chapter 5). Therefore, in Model B the setup with 3 m of clay cover between 2.6 and 1 Ma was used for calculating the time-integrated denudation rates of samples with a ^{26}Al/^{10}Be ratio below 5.4. The samples with higher ^{26}Al/^{10}Be ratios were also tested using Model B, and the results showed that the presence or absence of the early Quaternary clay cover had no influence on the outcome for these samples.

4.3.2. Loess cover and δ^{18}O threshold

The duration of loess cover is a direct function of the δ^{18}O threshold value, with higher values meaning longer periods of exposure and erosion at the surface (Fig. 6). In the following, we discuss these two terms through the total percentage of time spent covered/uncovered during the last 1 Ma.

The low δ^{18}O threshold values (Fig. 10B and C) suggest that all samples could have spent most of the last 1 Ma covered by loess (Table 3, Supplementary Table S5, Figs. 6 and 11 E, F). The differences between the δ^{18}O threshold values are manifested by the minimum time spent under loess cover, which varies between 24% and 97%. As expected, the samples with higher ^{26}Al/^{10}Be ratios (Model A) tend to have been covered for shorter time (20–60%), while the lower-ratio samples (Model B) are prone to spend most of the last 1 Ma covered by loess (74–97%).

The mean loess thickness was mostly above 6 m (Fig. 10A and C) with median values between ~11 m and 14 m (Supplementary Table S5). However, the thickness of the loess cover has minor effect on the modelled denudation rate (Fig. 10A), and the median value is influenced by the user defined upper threshold of 20 m. This lack of sensitivity of the model for the thickness of the loess cover can be explained by the change of CRN production pathways with subsurface

Table 3
Simple denudation rates calculated directly using the CRN concentrations of the samples and results of the MC modelling. For more details, please refer to Supplementary Tables S4 and S5. For a graph see Fig. 17. Simple denudation rates appear with their external uncertainties. Uncertainties of the uncovered bedrock erosion rates are calculated using the upper and lower quartiles. Min. loess cover: minimum percentage of time spent under loess cover during the last 1 Ma. Max int. erosion rate: time integrated surface denudation rate including both covered and uncovered periods during the last 1 Ma. Direct measure of the rock thickness removed by erosion (m) during this time.

Sample	Simple CRN-based						MC model results (for the last 1 Ma)					
	^{10}Be denudation rate			^{26}Al denudation rate			Setup	Uncovered bedrock denudation rate (m/Ma)			Min. loess cover	Max. int. erosion rate
	(m/Ma)			(m/Ma)				median	+	−	(%)	(m/Ma)
M01	28.9	±	2.9	42.7	±	6.3	B	50	10	5	92	3
M02	108.6	±	12.3	134.6	±	21.7	–	–	–	–	–	–
M03	45.0	±	4.4	63.6	±	9.8	B	102	30	15	85	10
M04	33.7	±	3.3	51.7	±	7.5	B	72	14	10	95	3
M05	24.0	±	2.2	37.8	±	5.4	B	35	4	3	97	1
M06	40.7	±	4.2	61.4	±	9.3	B	97	22	15	94	4
M07	37.1	±	3.5	48.9	±	7.2	B	63	12	7	74	1
M08	23.9	±	2.5	39.6	±	5.6	B	37	5	4	97	1
M09	19.1	±	1.8	23.3	±	3.2	A	21	2	2	38	14
M10	38.0	±	3.7	–		–	–	–	–	–	–	–
M11	30.2	±	2.8	–		–	–	–	–	–	–	–
M12	37.3	±	4.2	39.3	±	5.8	A	41	3	2	14	34
M13	42.9	±	5.2	64.1	±	10.5	B	103	28	19	79	14
M14	33.8	±	3.2	48.0	±	7.3	B	63	13	8	84	7
M15	28.9	±	3.5	36.1	±	5.5	A	32	3	3	18	26
M16	24.7	±	2.3	–		–	–	–	–	–	–	–
ACH	19.0	±	1.7	21.1	±	2.8	A	18	1	1	30	13
GUB	21.2	±	1.9	23.4	±	3.1	A	20	1	1	24	16
SP	30.9	±	2.8	37.1	±	5.2	A	30	2	2	46	17
VAD	35.5	±	3.2	43.6	±	6.2	A	35	2	3	60	15

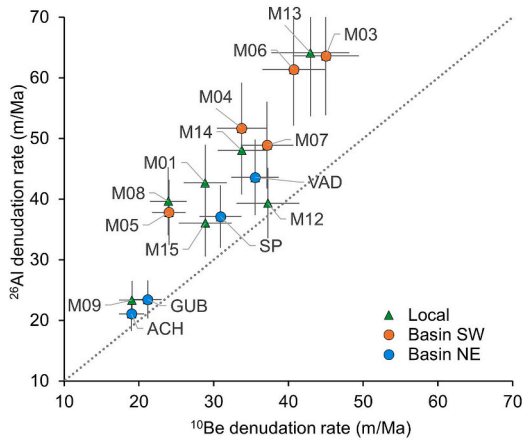

Fig. 8. Comparison plot of simple ^{10}Be and ^{26}Al bedrock denudation rates. Note that the samples with ^{26}Al/^{10}Be ratios close to the surface production rate ratio are more similar (plot closer to the grey dotted line of equivalent values), while low ratio samples show larger discrepancies evidencing a disequilibrium between their CRN inventories.

depth. For a loess cover of 1, 2 and 3 m, ~38, ~15 and ~ 6% of the total surface production remains, respectively, while at 10 and 20 m this value reduces to ~0.8 and ~ 0.5%, respectively. This limited increase of shielding with depth over 3 m loess cover is due to the predominance of the weakly attenuated muogenic production at this depth range (Braucher et al., 2003, 2011; Balco, 2017).

4.3.3. *Denudation rates of the uncovered bedrock*

The modelled uncovered bedrock denudation rate varied between 103 $^{+28}/_{-19}$ m/Ma and 18 ± 1 m/Ma. For local samples, this value varies between 21 ± 1 m/Ma and 103 $^{+28}/_{-19}$ m/Ma, for CW samples in the southwestern area between 102 $^{+30}/_{-15}$ m/Ma and 35 $^{+4}/_{-3}$ m/Ma, while it was lower in the northeastern catchments (between 35 $^{+2}/_{-3}$ m/Ma and 18 ± 1 m/Ma) (Fig. 11A,B). The distinction is more characteristic between the samples that spent longer time uncovered (Model A) compared to those spending most of the Quaternary covered (by clay and then loess; Model B). The former group tends to have lower uncovered denudation rates, while the mostly covered areas appear to have higher uncovered denudation rates. However, in this group there are some low-rate exceptions overlapping with the first group (M05, M08) (Supplementary Table S5; Fig. 12A and B).

If we take a closer look at the ^{26}Al/^{10}Be ratios and the CRN concentrations, we get an explanation for the variability of the uncovered bedrock denudation rates. Based on their CRN ratios, the Model A and Model B groups are well differentiated (Fig. 12A). Samples with higher CRN concentrations among the areas with the longest enduring loess cover have lower denudation rates, and thus lower uncovered bedrock denudation rates overlap with values of the more exposed group (M05, M08; Fig. 12A and B).

4.3.4. *Integrated bedrock denudation rates: a measure of surface lowering*

The bedrock denudation rates modelled for the periods spent uncovered (Figs. 11A and B, 12A and B) are not relevant as long-term bedrock denudation rates of the study area. To get an impression on the rate of surface lowering during the last 1 Ma, the periods spent uncovered (zero erosion) had to be integrated with the exposed timespans (Fig. 11C, D, E and F). The integrated denudation rate (m/Ma) is the erosion rate that encompasses the periods spent both covered and uncovered by loess at a given sample site or catchment, which is a direct measure of the thickness of rock (m) removed during the last 1 Ma (Fig. 13).

The rock thickness eroded from the bedrock surface of the areas covered by loess for over 70% of time usually remains under ~5 m (Model B). This value is surpassed only for three samples (M14, M03 and M13: 7, 10 m and 14 m, respectively). From the areas that were covered for shorter time, a minimum thickness of ~13–17 m was eroded (Model A). For two samples, which were loess-covered for less than 200 ka during the last 1 Ma, the rock thickness removed was considerably larger: ~26 and ~ 34 m (M15 and M12, respectively) (Fig. 13A).

A comparison of the uncovered and integrated bedrock denudation rates shows that surface lowering by denudation can be highly overestimated using the uncovered rates, especially in the case of areas characterized by long-time shielding under loess (Fig. 13B). The

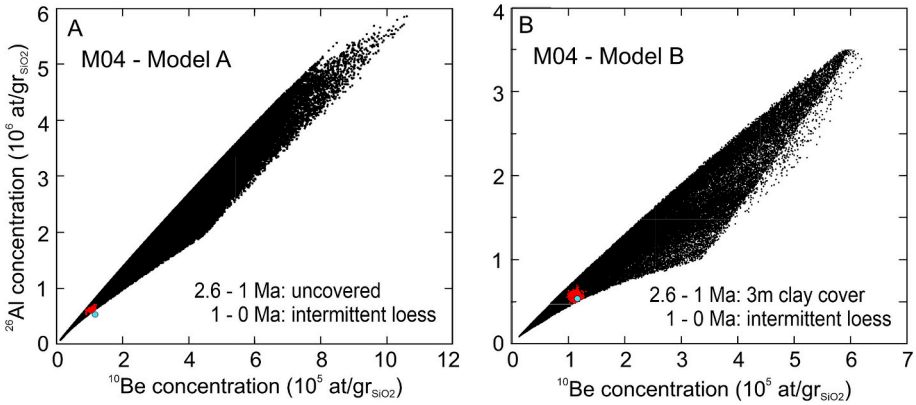

Fig. 9. ^{26}Al and ^{10}Be concentration simulation results (black dots), among which the ones coloured with red were acceptable for being within uncertainties of the measured concentrations (blue dot). Examples of an unacceptable (A) and an acceptable (B) model fit for a low ratio sample (M04). Model A: with the surface uncovered and Model B: with the surface covered by 3 m clay before the onset of loess deposition (2.6–1 Ma). (For interpretation of the references to colour in this figure legend, the reader is referred to the web version of this article.)

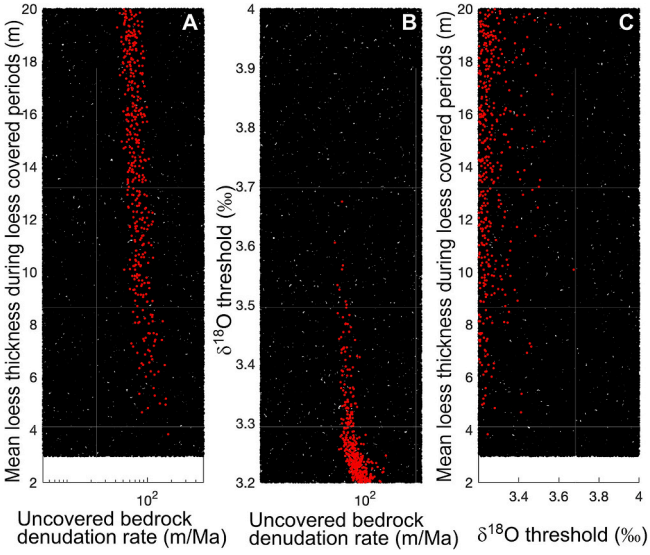

Fig. 10. Simulation results for the M04 sample showing the uncovered bedrock denudation rate, mean loess thickness and δ^{18}O threshold values. Red dots are the acceptable values. A and B: The mean loess thickness and the δ^{18}O threshold plotted against the uncovered bedrock denudation rates. C: The mean loess thickness plotted against the δ^{18}O threshold values. (For interpretation of the references to colour in this figure legend, the reader is referred to the web version of this article.)

modelled uncovered denudation rates are ~7 to 53 times larger for this sample group. The modelled uncovered and integrated bedrock denudation rates are much closer for the areas spending less time under a loess cover, with a maximum 2.4 times difference.

5. Discussion

5.1. Present day extent of loess cover and modelled percentage of loess cover

The percentage of present-day loess cover, estimated based on the geological map (Fig. 5B), is 40–90% in the southwestern catchments and 0–42% in the northeastern areas (Fig. 14). An almost continuous loess cover over the last 1 Ma was suggested by the model for the westernmost, low-elevation catchments (74–97%) with the highest values for CW samples M04, M05 and M06, and for local samples M01 and M08 coming from low lying smooth ridges (~92–97% of the total time). These samples provided reasonable model fit only with the introduction of a clay cover before the onset of loess formation (Model B). Longer uncovered periods were allowed only for the samples coming from higher elevations. Nevertheless the above results suggest that at least after several thousand years of warm, interglacial conditions there was room for a period of exposure and CRN production even in catchments of high percentage of loess cover, which is consistent with modern observations of the loess cover being thinned and constantly eroded, and with the current absence of loess cover at the sampled sites.

Both local and CW samples from the highest elevations could be loess covered for not more than ~50% of time during the last 1 Ma and these sample locations are those that could be modelled being exposed before the onset of loess deposition (Model A). However, there are some exceptions: sample M09 could be uncovered for >60% of time, thus it belongs to this group, despite its position on a low-lying ridge. On the contrary, M13 and M14 are suggested to be loess covered for at least ~80% of time (Model B), in spite of their position on top and base of tor-like rock formations and at relatively high elevations (>400 m asl) (Figs. 2, 3H, I, 4 and 14; Tables 3, S5). It is possible, however, that uneven erosion processes at these sites, like chipping and/or exfoliation along bedding planes led to the relatively low CRN concentrations and ratio of these samples. This may also be reflected by the model results, suggesting relatively high uncovered bedrock denudation rate for these samples (Fig. 13B).

5.2. How large is the bias between the simple and MC modelled denudation rates?

The modelled uncovered bedrock denudation rates match the simple ^{10}Be denudation rates for the Model A sample group, but the modelled values for the Model B group are higher than the simple rates by up to a factor of 2.4 for ^{10}Be and 1.6 for ^{26}Al (Fig. 15A). However, the time-integrated denudation rates, representative of the long-term lowering of the bedrock surface, could be strongly overestimated by the simple CRN denudation rates especially for samples belonging to the Model B group (Fig. 15B).

While for Model A, the simple ^{10}Be denudation rates are not exceeding the MC modelled time-integrated rates by more than 2.4 times, for the Model B they are usually 4 to 12 times larger, with some samples up to 22–31 time larger values (M05, M07 and M08; Fig. 15B). The observed pattern is similar for both nuclides (Table 3, Supplementary Tables S4 and S5).

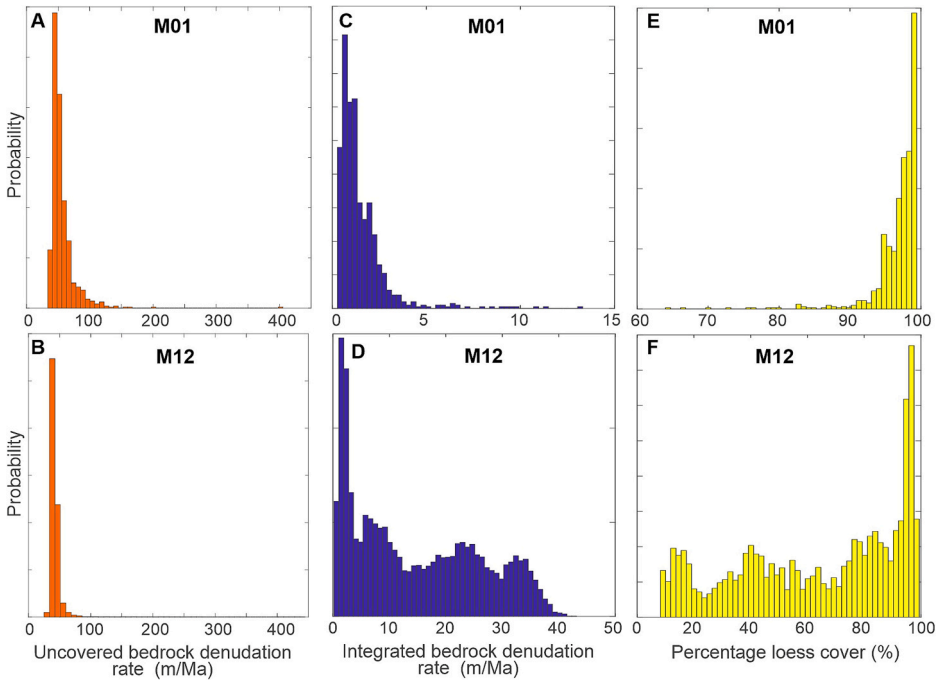

Fig. 11. Probability distribution plots showing the uncovered and integrated bedrock denudation rates during the last 1 Ma (A-B and C—D, respectively) and the percentage of time spent under loess cover during the last 1 Ma (*E*- F). Examples of the M01 (A,C,E) and the M12 (B,D,F) samples (low and high $^{26}Al/^{10}Be$ ratios, respectively). Note that higher loess coverage of low ratio samples implies low integrated denudation rates, even with potentially higher uncovered bedrock denudation rates.

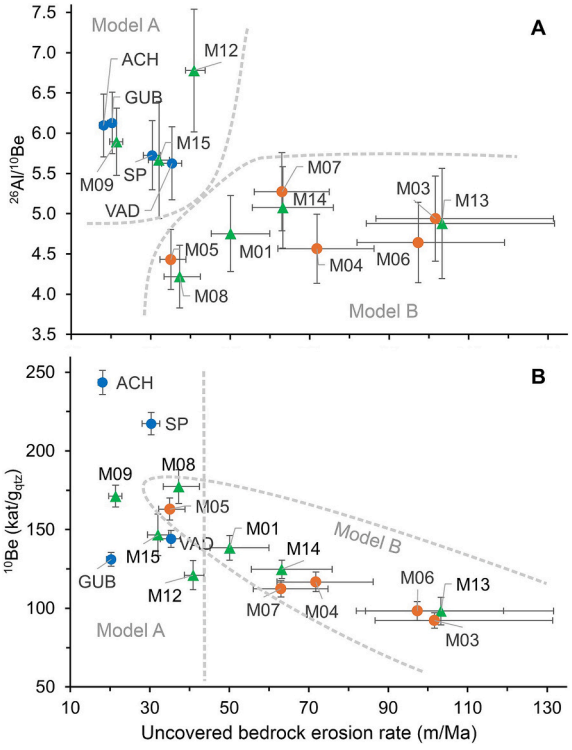

Fig. 12. Relationship between the uncovered bedrock denudation rate and (A) the $^{26}Al/^{10}Be$ ratio; and (B) the ^{10}Be concentration, during the last 1 Ma. For data refer to Tables 1, 3, Supplementary Tables S2, S4, S5. Note that the two model scenarios could be well distinguished based on the CRN ratios, but the nuclide concentrations themselves are insufficient to separate the two groups.

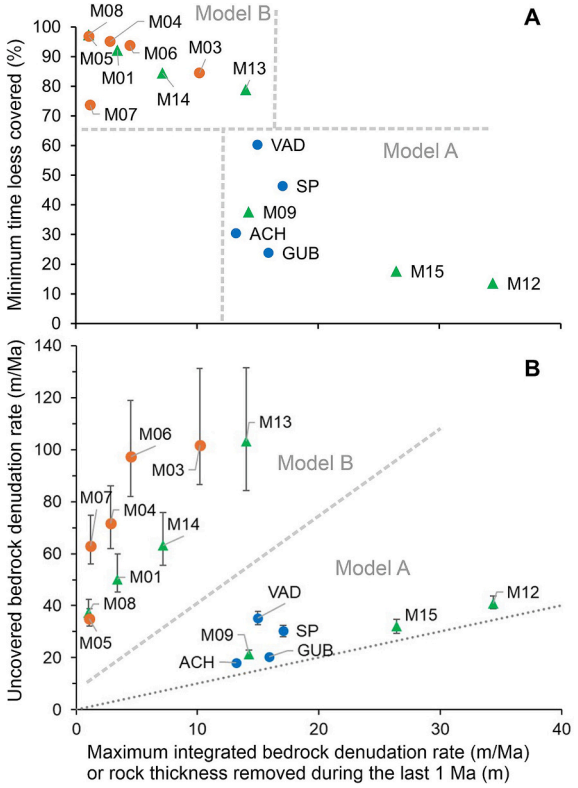

Fig. 13. Relationship between the rock thickness removed during the last 1 Ma (equivalent to the integrated denudation rate) and (A) the minimum time spent loess covered; and (B) the bedrock denudation rate during the uncovered periods. For data refer to Table 3, Supplementary S5. Dotted line in inset B is plotted where uncovered and maximum integrated bedrock denudation rates are equal.

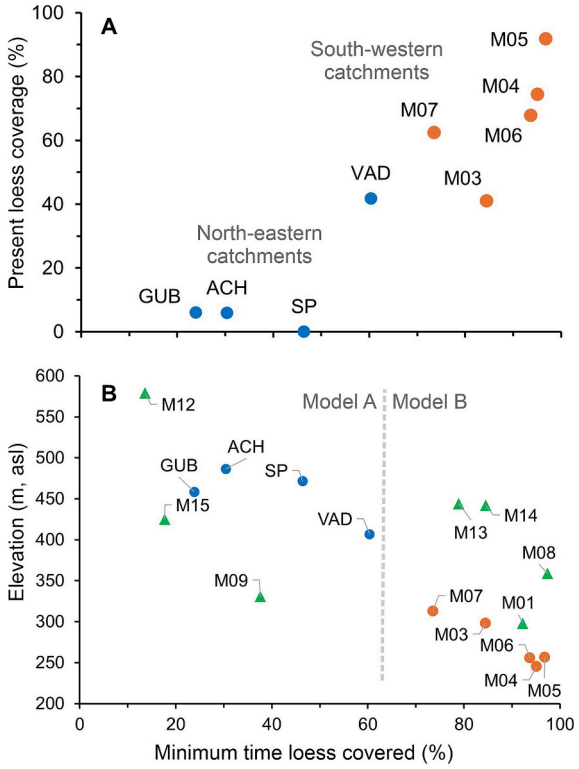

Fig. 14. Minimum time spent under loess cover during the last 1 Ma compared (A) to the present-day loess coverage (only for catchments), and (B) to the sample elevation (catchment mean elevation for CW samples). Dots are CW samples (blue: northeastern area, orange: southwestern area), green triangles are local samples. For data refer to Table S5. Note that Model A and B samples are well distinguished by their position on the plot. (For interpretation of the references to colour in this figure legend, the reader is referred to the web version of this article.)

5.3. *The thickness of bedrock removed during the last 1 Ma*

As discussed above, the rock thickness removed during the last 1 Ma is best estimated using the integrated bedrock denudation rates that account for periods with shielding and zero erosion as well as periods with erosion and no shielding. The estimated mean thickness of rock removed is 15 ± 2 m for the northeastern catchments, 4 ± 4 m for the southwestern catchments and 14 ± 12 m for the local samples. The high scatter of the local samples stems form the fact that part of them belongs to Model A and others to Model B. Thus, it seems again to be more appropriate to use these clusters instead of the local versus CW samples. The maximum surface lowering by erosion for catchments and ridges belonging to Model A was 19 ± 8 m/Ma, while for Model B it was only 5 ± 5 m/Ma (Table 3, Supplementary Table S6, Fig. 13).

If the the simple ^{10}Be denudation rates were considered, the estimated mean rock thickness removed during the last 1 Ma would be 27 ± 8 m and 35 ± 8 m for Model A and Model B areas, respectively (Table 3, Supplementary Table S6). In this approach the climate oscillations and the shielding effect of the Quaternary loess cover are ignored and the amount of surface denudation is overestimated by a factor of ~1.4 for the less shielded group, and by a factor of ~7 for areas with the most enduring loess covers. If simple ^{10}Be and modelled integrated denudation rates are compared for each sample, five samples show a minor bias, i.e. have similar simple ^{10}Be and integrated bedrock denudation rates (Fig. 15B). These samples coincide with the ones that have spent less than 30% of the time covered by loess and have matching uncovered rates (Figs. 14A and B; 15A; M09, M12, M15, GUB, ACH). This value may be regarded as the threshold above which the shielding of the surface must not be ignored during the quantification of bedrock

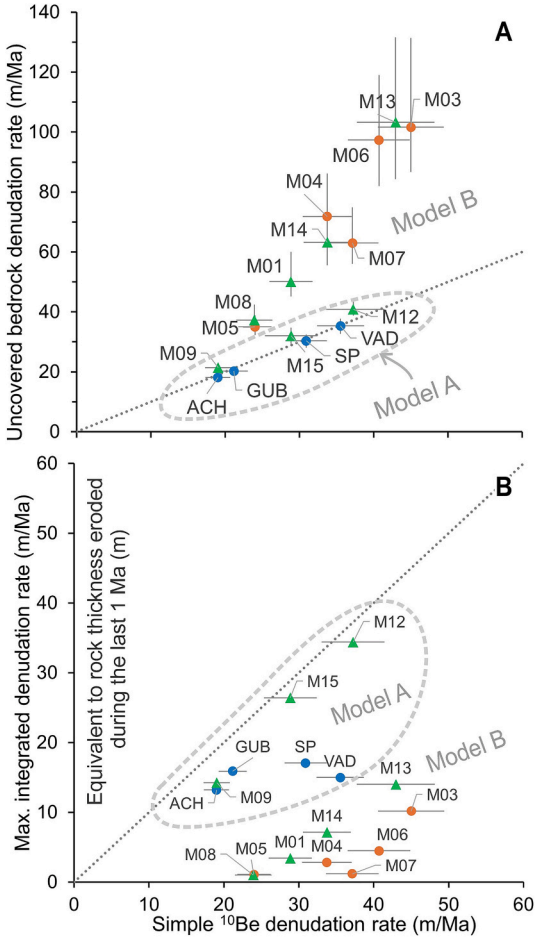

Fig. 15. Comparison of the simple ^{10}Be denudation rates with the MC modelled (A) uncovered bedrock denudation rates and (B) time integrated denudation rates for the last 1 Ma. For data refer to Table 3.

denudation processes. This shielding threshold may be applicable not only for loess but also for intermittent snow, sediment, and soil cover, thick enough to hinder or stop CRN production.

The mean slope of the catchments varies between 7° and 14° and it shows no correlation with the estimated denudation rates or rock thickness eroded (Fig. 16A). An increase of the rock thickness removed with elevation can be observed, but this correlation is rather due to the increasing time spent exposed with the elevation (Fig. 16B). In other words, the loess cover in the study area decreases with elevation and the resulting longer exposure time leads to larger thickness of rock eroded.

5.4. *MC modelled denudation rates corrected for the shielding effect of the loess*

The apparent simple ^{10}Be denudation rates were between ~24 and 45 m/Ma for Model B and 19 to 37 m/Ma for the more exposed Model A samples. These values are relevant for the last 20–30 ka, an integration time that was not available in the WM due to the loess cover of the surface. Therefore, steady-state CRN concentrations could not be reached. The simple ^{26}Al denudation rates are exceeding the ^{10}Be denudation rates due to the faster decay of ^{26}Al (Figs. 8 and 17). The overestimation of the denudation rate is proportional to the former shielding by loess: shorter loess covers result in smaller disequilibrium between the two nuclides (Figs. 14 and 15). Following the same line of thought, the simple denudation rates for these samples provide a better estimate of the long-term bedrock denudation rates (modelled time-integrated denudation rates) as well. This difference is visualized by

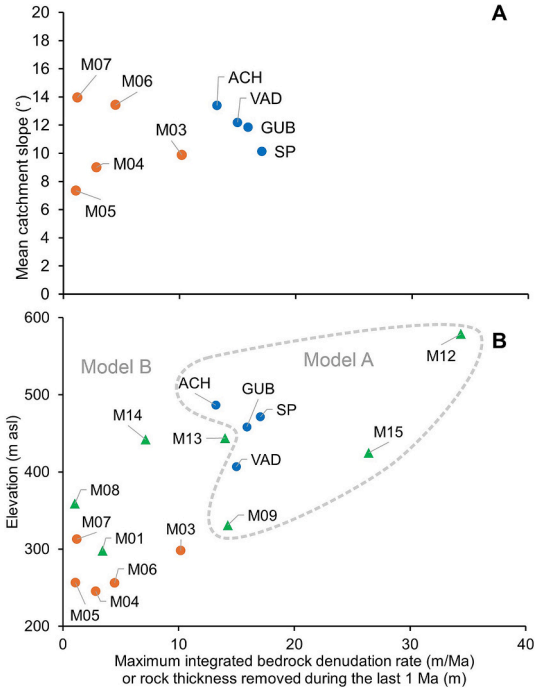

Fig. 16. Modelled thickness of bedrock removed by surface denudation plotted against (A) Mean catchments slope and (B) sample elevation (for catchments mean catchment elevation). For data refer to Table 3.

comparing the Model A and B denudation rate values in Fig. 17. The "standard" approach using the simple ^{10}Be denudation rates would lead to mean values of 27 ± 8 m/Ma and 34 ± 8 m/Ma for Model A and B samples respectively, while the MC modelled integrated values are only 19 ± 8 m/Ma and 5 ± 5 m/Ma, respectively (Fig. 18A; Supplementary Table S6). Accordingly, for the Model A (less covered) group the best estimate (MC modelled) denudation rates were 1.1–2.4 times (mean: 1.5 ± 0.5) overestimated by the simple ^{10}Be denudation rates due to the loess cover. The same overestimation was much larger for the areas that spent most of the time loess covered (Model B) with simple ^{10}Be rates 3–31 times larger than the MC modelled values (mean: 13 ± 10) (Fig. 18A; Supplementary Table S6).

Depleted ^{26}Al/^{10}Be ratios due to glacial shielding were also noted in a study of paired ^{26}Al and ^{10}Be CW denudation rates in the Vosges Mountains (Germany) (Jautzy et al., 2024). They compared the unglaciated northern catchments to the previously glaciated southern areas. In the former, they found steady-state CRN concentrations with denudation rates between ~34 and 73 m/Ma for both nuclides. However, in the southern catchments the ^{26}Al/^{10}Be ratios were below the surface value, indicative of considerable past burial. They emphasized the importance of the application of both ^{26}Al and ^{10}Be nuclides to reveal past shielding of the surface and suggested to exclude catchments with ^{26}Al/^{10}Be disequilibrium if regional conclusions are based on the factors controlling Holocene denudation processes. However, they did not attempt to quantify the most probable long-term denudation rate of their study area by using the glacial record and both nuclides data.

Meyer et al. (2010a) studied CW ^{10}Be denudation rates of two catchments in the northeast part of the Rhenish Massif, an area of prolonged slow Cenozoic uplift lying within the Western European loess domain (Lehmkuhl et al., 2021). Most of the ^{10}Be denudation rates range from 47.6 ± 5.5 m/Ma and 65 ± 14 m/Ma, comparable to the long-term uplift rate of the area (~50 m/Ma) suggesting a steady-state landscape. However, the short-term erosion rates quantified by sediment trapping are much lower; they range from 9 to 25 m/Ma. For this discrepancy, several factors have been invoked, among which the most plausible is that the rare flood events may not be captured in the short-term records. However, it is also possible that the shielding effect of the intermittent loess cover could also play a role in the lowered ^{10}Be signal and the resulting higher ^{10}Be denudation rate estimates.

Halsted et al. (2025) provided a global revision of published denudation rates in large and medium sized catchments. They found that paired nuclide CW denudation rates suggest a discrepancy between the ^{26}Al and ^{10}Be rates, appearing in nearly one third of the catchments. In those settings ^{26}Al/^{10}Be ratios are lowered, manifested in higher apparent CW denudation rates for ^{26}Al compared to ^{10}Be based rates. This discrepancy stems from the storage of the sediment on hillslopes or within the fluvial system during transport for long enough time compared to the half-lives of the cosmogenic nuclides, leading to lowered CRN ratios (Wittmann and von Blanckenburg, 2016). Variable CRN erosion rates inferred from multi-nuclide studies revealed sediment storage for instance in the Bolivian Andes (Hippe et al., 2012), in the Amazon Basin (Wittmann et al., 2011) or at the passive margin of Western Australia (Fülöp et al., 2020).

Schaller et al. (2001 and 2016) investigated CW ^{10}Be denudation rates of large rivers and their tributaries in Central Western Europe, at comparable latitudes and elevations to our study area. They found that denudation rates were 21–28 m/Ma in the Regen, ~43–101 in the Neckar, 14–26 m/Ma in the Meuse and Vltava and 5–72 m/Ma in the Allier-Loire catchments. These rates are within the same order of magnitude as the simple ^{10}Be denudation rates of our study area, and 2–5 times higher than the MC modelled time-integrated rates for Model A and 4–20 times higher than those for Model B samples in the Western

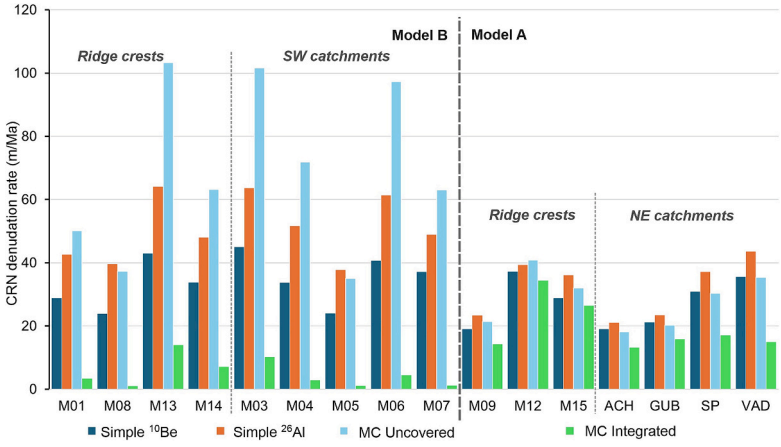

Fig. 17. Comparison of the outcomes of the simple ^{10}Be, ^{26}Al and MC modelled ^{26}Al/^{10}Be uncovered and integrated denudation rates for local and CW samples of the Model A and Model B groups. For data refer to Table S5. For mean values refer to Fig. 18A and Supplementary Table S6.

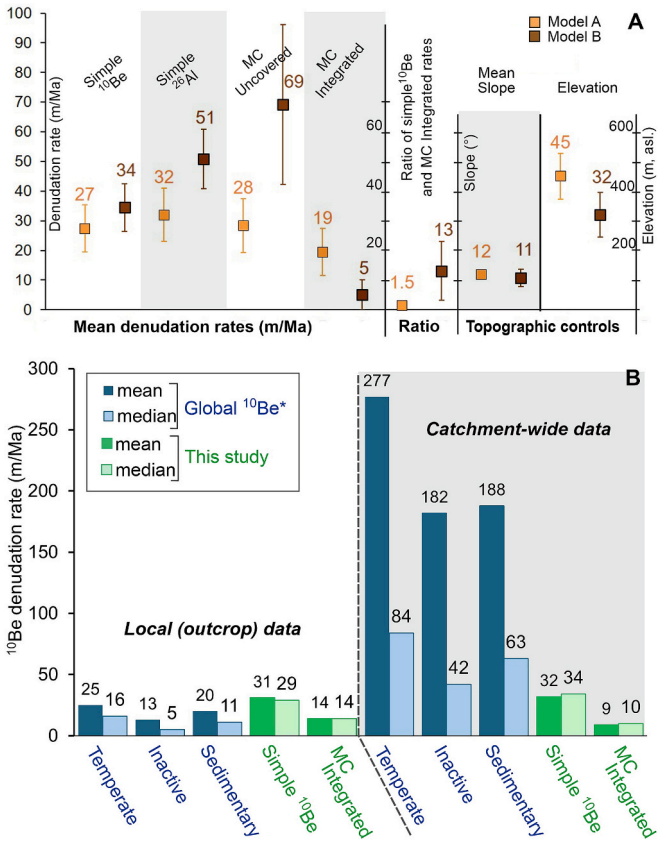

Fig. 18. Summary of the results. (A) Comparison of the Model A and Model B outcomes of the mean denudation rates together with some topographic factors of the sample site, which may control the denudation rates. Bias means the factor by which the simple ^{10}Be denudation rates overestimated the MC modelled integrated denudation rates. (B) Comparison of the local versus catchment-wide denudation rates of the global mean and median ^{10}Be denudation rates for temperate, inactive and sedimentary settings (Portenga and Bierman, 2011) with the simple ^{10}Be and MC modelled ^{26}Al/^{10}Be integrated denudation rates of this study. For data refer to Supplementary Table S6.

Mecsek Mts. Like Meyer et al. (2010a), they also found that the ^{10}Be CW denudation rates were 1.5–4 times larger than the rates derived from the measured river load. Drainage areas of the Neckar, Regen and Meuse rivers are located within the Western European loess domain, and are partly covered by loess (Lehmkuhl et al., 2021). So again, the partial shielding of loess in these areas could also be invoked as a possible reason for the higher ^{10}Be derived denudation rates.

5.5. Controls on the denudation rate and relief evolution

Several studies have shown that tectonic uplift, lithology, climate, and topographic factors (Norton et al., 2011; Portenga and Bierman, 2011; Dixon et al., 2016; Jautzy et al., 2024; Schaller et al., 2025) represent the main controls on the denudation rates. Olivetti et al. (2016) examined CW ^{10}Be denudation rates in small, mid-latitude catchments in the French Massif Central, at similar settings to the WM but with no loess deposits. They found that CW denudation rates varied between 40 and 80 m/Ma, similar to the simple ^{10}Be denudation rates, but much higher than the MC modelled values in our study area. However, the French Massif Central has a higher topography and precipitation compared to the WM, which makes it more prone to surface denudation. If the simple ^{10}Be denudation rates were used in our study area, neglecting the temporal loess cover, this difference of denudation rate between the two areas would have remained hidden.

In the Harz Mts (Germany), CW denudation rates were determined in small catchments developed on granitic lithology of comparable size to those in our study (Hetzel et al., 2024). CW ^{10}Be denudation rates (n = 10) varied between ~24 and 55 m/Ma with higher rates in the steeper catchments. Besides, two samples from the drainage divide also yielded ~20 m/Ma denudation rates. Catchments with a similar slope to our study area had denudation rates of ~30 m/Ma, values very similar to the simple denudation rates and for the uncovered denudation rate of the Model A samples in our study area. The Harz Mts were in the periglacial climate zone with reworked loess sediments on the slopes, but typical loess sediments are missing (Lehmkuhl et al., 2021). The similar denudation rates observed on similar slopes in the more humid granitic Harz Mts compared to the continental, sedimentary WM suggest that the slope plays a considerable role in setting the speed of denudation processes.

Similar CW ^{10}Be denudation rates (22–51 m/Ma) of small drainage basins (n = 20) were found in the Bohemian Massif, an area of comparable tectonic, topographic, and climatic setting to the WM, where the steep catchments and those with less resistant lithologies eroded twice as fast as those of gentle slopes and/or of harder rocks (Robl et al., 2024). It has to be mentioned that the Bohemian Massif is also affected by Quaternary loess formation (Lehmkuhl et al., 2021), thence a certain degree of CRN disequilibrium in some catchments cannot be excluded. This may also explain some of the outliers and the weaker correlation to topographic metrics observed in some catchments.

Aiming at an overview of the WM denudation rates in a global perspective, they were compared with the ^{10}Be denudation rates of temperate, tectonically inactive settings and on sedimentary lithologies, summarised by the comprehensive study of Portenga and Bierman (2011) (Fig. 18B, Supplementary Table S6). There is a considerable difference between local (outcrop) and CW samples in the dataset, with the CW data being much higher. This difference is absent in the WM. The CW ^{10}Be denudation rates of the study area are much slower than the world-wide mean and median values. Nevertheless, the local data of the global compilation are like the mean and median MC modelled integrated denudation rate of the WM. The simple local ^{10}Be denudation rates, which are not corrected for the shielding effect of the loess, in the WM are somewhat above the global values, an artefact that would have remained hidden in case of using a single nuclide in our study area.

Mean ^{10}Be denudation rates in the global compilation are strikingly above the median values for the CW denudation rates. For the local data, this difference also exists, but it is much smaller. This positive skewness of the global data is absent from our study area for both CW and local data. This means that the global dataset includes some study areas with extremely fast denudation rates, which are obviously absent in our small and homogeneous study area (Fig. 18A, and see also section 5.3 on topographic control).

5.6. Comparison of the relief evolution of the WM to similar settings

The long-term rate of relief evolution in the WM was assessed using the MC modelled integrated denudation rates on ridge bedrock and stream sediment samples. The first observation is that the lowering rate of the ridge crests was similar to the mean denudation rate of the catchments with values of 14 ± 12 and 9 ± 7 m/Ma, respectively (Supplementary Table S6, Fig. 18B). Accordingly, the ridges are eroding at a similar rate, or slightly faster compared to the entire drainage basins suggesting a relatively steady landscape in the study area during the last 1 Ma. An analogous pattern was observed in the above-mentioned study of the Harz Mts (Germany), where CW denudation rates were similar or slightly faster than the lowering of the ridges (Hetzel et al., 2024).

In the Black Forest, southwest Germany, spatially averaged ^{10}Be denudation rates of small catchments along the Acher and Guttach rivers and local samples from the bounding ridge crests were all higher than those found in the WM (Meyer et al., 2010b). Unlike in our study, they found that in most drainage basins, the erosion of the ridge crests was slower than that of the spatially averaged CW rates (34–59 m/Ma and 52–91 m/Ma, respectively), suggesting an increase of the relief of 24 ±

12 m/Ma. The differential landscape evolution was absent only in the flat south-western part of the Guttach drainage basin, where both the local and the CW denudation rates were ~ 40–50 m /Ma. This area is a relatively high (~900–1000 m asl) low-relief landscape, which has not yet been reached by the backwards migration of the knickpoint of the Guttach river. The higher elevation and precipitation of this area explain the faster denudation rates compared to our study area in a more continental setting.

6. Concusions

Due to the shielding effect of an intermittent loess cover, typical in the Western Mecsek Mts, the simple cosmogenic denudation rates calculated using ^{10}Be and ^{26}Al nuclides are divergent. A Monte Carlo modelling approach using both ^{26}Al and ^{10}Be data was designed to quantify the duration of the former loess cover in light of the climate oscillations during the last 1 Ma and to estimate the bedrock denudation rates corrected for the shielding by loess. This is the first study that examines the influence of past loess cover on CRN concentration in bedrock and stream sediment samples and to quantify the denudation rates corrected for this shielding. The provided methodology can be used in other settings where an intermittent cover (loess, soil snow or ice) could have led to a decreased CRN ratio, enabling to find the real controlling factors of landscape evolution through estimating the cover-corrected bedrock denudation rates and also the past extent of the cover.

Our main conclusions are as follows:

- Time-integrated denudation rates calculated with the new MC model approach provide the most realistic long-term denudation rates and relieve the discordance between denudation rates derived from single ^{10}Be and ^{26}Al concentrations.
- In the Western Mecsek Mts the MC-modelled integrated bedrock denudation rates are slow: ~1–34 m/Ma, with a mean of 5 ± 5 m/Ma and 19 ± 8 m/Ma for areas with loess cover below and over ~60% of the time, respectively (Figs. 18 and 19)
- The "standard" single nuclide, simple ^{10}Be denudation rates overestimate the true rate of bedrock erosion. This overestimation is larger (up to ~30×) for areas characterized by more enduring loss covers (Figs. 17, 18 and 19).
- The denudation rate is similar, or only slightly faster on the ridges compared to the catchment mean values. (Figs. 17, 18 and 19)
- There is an increase of denudation rates with elevation, which trend is parallel with the decrease of loess cover on more elevated areas (Figs. 14, 16 and 19).
- The modelled slow denudation rates agree with the maximum incision rate estimates of 8–35 m/Ma derived from local loess stratigraphical data (Sebe et al., 2025) and support moderate uplift rate of the Western Mecsek Mts.
- In terms of the safety of the planned radioactive waste disposal facility, the MC-modelled time-integrated denudation rates guarantee that the planned minimum 500 m subsurface depth of the repository is safe and will not be threatened by exhumation due to denudation of the area, remaining well below one meter in the given timespan (maximum denudation is 30 cm in 10 kyrs).

Some key perspectives for future studies:

- In formerly non-glaciated areas, the loess cover can act as a significant shielding factor for CRN applications and has to be accounted for.
- If the overestimation of denudation rates caused by the intermittent shielding of the surface is neglected, the inferences regarding the geomorphic, tectonic, and climatic controls on landscape evolution may be biased.
- We suggest the systematic use of a paired ^{26}Al and ^{10}Be approach to test the steady-state assumption not only in large river catchments prone to prolonged sediment storage and in formerly glaciated areas, but also in study areas where earlier sediment covers could have been long enough to effectively modify the CRN ratio within the bedrock surface.

CRediT authorship contribution statement

Zsófia Ruszkiczay-Rüdiger: Writing – review & editing, Writing –

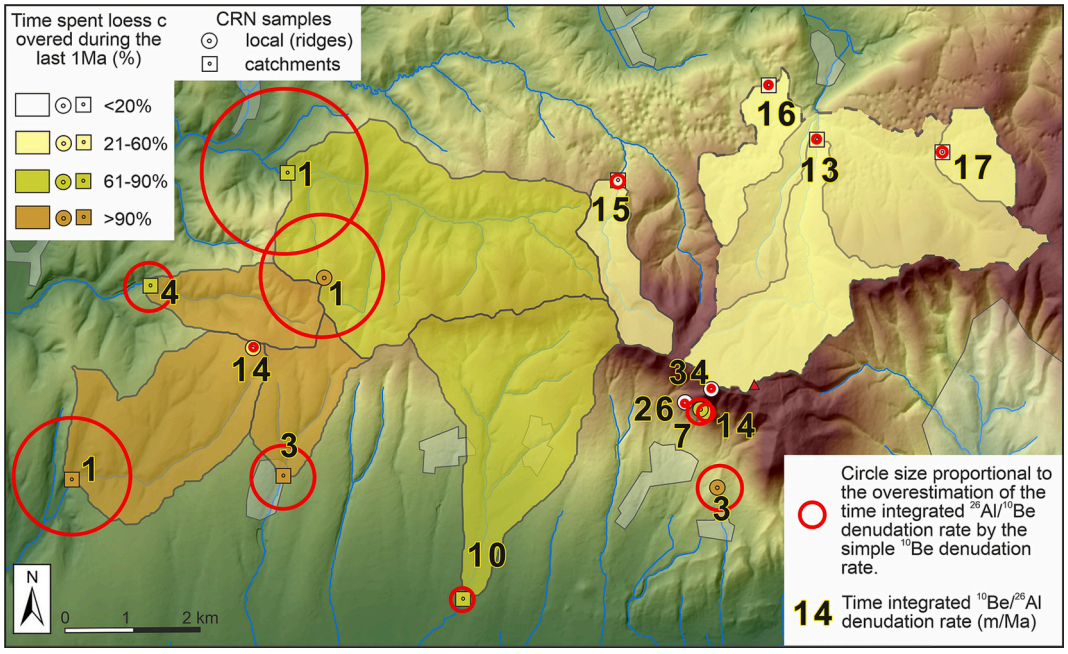

Fig. 19. Percentage of loess cover, MC modelled time integrated ^{26}Al/^{10}Be denudation rates and the magnitude of overestimation of the modelled denudation using the single nuclide ^{10}Be denudation rates of the studied catchments and ridges plotted on the digital elevation model of the study area. Note that the simple ^{10}Be denudation rates yielded a good estimate on the long-term denudation rate for the areas covered by loess for less than 60% of time. The overestimation could be much larger for areas with more enduring loess cover.

original draft, Visualization, Validation, Project administration, Methodology, Investigation, Funding acquisition, Formal analysis, Data curation, Conceptualization. **Mads Farschou Knudsen:** Writing – review & editing, Visualization, Software, Methodology, Investigation, Formal analysis, Data curation. **Márton Bauer:** Writing – review & editing, Visualization, Software, Conceptualization. **Tamás Telbisz:** Writing – review & editing, Visualization, Formal analysis, Data curation. **A.S.T.E.R. Team:** Writing – review & editing, Writing – original draft, Visualization, Validation, Project administration, Methodology, Investigation, Funding acquisition, Formal analysis, Data curation, Conceptualization. **Krisztina Sebe:** Writing – review & editing, Visualization, Validation, Supervision, Software, Data curation, Conceptualization.

Declaration of generative AI and AI-assisted technologies in the writing process

During the preparation of this work the authors did not use AI tools.

Declaration of competing interest

The authors declare that they have no known competing financial interests or personal relationships that could have appeared to influence the work reported in this paper.

Acknowledgements

Funding: PURAM, Mecsekérc Ltd. (BAF-I-5/2016), NKFIH project FK 124807 and HAS. Sample processing: Cosmogenic Laboratories of Budapest ($n = 16$) and of the University of Edinburgh ($n = 4$); AMS measurements: ASTER, Aix en Provence (n = 16) and SUERC, Glasgow (n = 4).

Sample processing at the Cosmogenic Nuclide Laboratory of the University of Edinburgh was carried out by Elaine McDougall under the guidance of Andrew Hein. The AMS at the SUERC AMS Laboratory were carried out under the guidance of Derek Fabel and Andy Hein.

We are grateful to two anonymous Reviewers and our Editor, Tobias Sprafke for their comments that helped to improve the ms. This is HUN-REN - MTM – ELTE Paleo contribution No. 438.

Appendix A. Supplementary data

Supplementary data to this article can be found online at https://doi.org/10.1016/j.catena.2026.109971.

References

Andersen, J., Egholm, D.L., Knudsen, M.F., Linge, H., Jansen, J.D., Pedersen, V.K., Nielsen, S.B., Tikhomirov, D., Olsen, J., fabel., D., Xu, S., 2018. Widespread erosion on high plateaus during recent glaciations in Scandinavia. Nat. Commun. 9 (1), 830. https://doi.org/10.1038/s41467-018-03280-2.

Arnold, M., Merchel, S., Bourlès, D.L., Braucher, R., Benedetti, L., Finkel, R.C., Aumaître, G., Gottdang, A., Klein, M., 2010. The French accelerator mass spectrometry facility ASTER: improved performance and developments. Nucl. Instruments and methods in Phys. Res. B 268, 1954–1959. https://doi.org/10.1016/j.nimb.2010.02.107.

Balco, G., 2017. Production rate calculations for cosmic-ray-muon-produced ^{10}Be and 26Al benchmarked against geological calibration data. Quat. Geochronol. 39, 150–173. https://doi.org/10.1016/j.quageo.2017.02.001.

Bierman, P., Steig, E.J., 1996. Estimating rates of denudation using cosmogenic isotope abundances in sediment. Earth Surf. Process. Landf. 21 (2), 125–139. https://doi.org/10.1002/(SICI)1096-9837(199602)21:2<125::AID-ESP511>3.0.CO;2-8.

Bierman, P., Turner, J., 1995. ^{10}Be and ^{26}Al evidence for exceptionally low rates of Australian bedrock erosion and the likely existence of pre-Pleistocene landscapes. Quat. Res. 44 (3), 378–382. https://doi.org/10.1006/qres.1995.1082.

Bierman, P.R., Caffee, M.W., Davis, P.T., Marsella, K., Pavich, M., Colgan, P., Mickelson, D., Larsen, J., 2002. Rates and Timing of Earth Surface Processes from In Situ-Produced Cosmogenic Be-10. Mineralogy, Petrology, And Geochemistry. Mineralogical Soc. America, Washington, Beryllium, pp. 147–205. https://doi.org/10.2138/rmg.2002.50.4.

Bierman, P.R., Nichols, K., K., 2004. Rock to sediment – slope to sea with ^{10}Be – rates of landscape change. Annu. Rev. Earth Pl. Sc. 32, 215–255. https://doi.org/10.1146/annurev.earth.32.101802.120539.

Borchers, B., Marrero, S., Balco, G., Caffee, M., Goehring, B., Lifton, N., Nishiizumi, K., Phillips, F., Schaefer, J., Stone, J., 2016. Geological calibration of spallation production rates in the CRONUS-Earth project. Quat. Geochronol. 31, 188–198. https://doi.org/10.1016/j.quageo.2015.01.009.

Braucher, R., Brown, E.T., Bourlès, D.L., Colin, F., 2003. In situ produced ^{10}Be measurements at great depths: implications for production rates by fast muons. Earth Planet. Sci. Lett. 211 (3–4), 251–258. https://doi.org/10.1016/S0012-821X(03)00205-X.

Braucher, R., Merchel, S., Borgomano, J., Bourles, D.L., 2011. Production of cosmogenic radionuclides at great depth: a multi element approach. Earth Planet. Sci. Lett. 309, 1–9. https://doi.org/10.1016/j.epsl.2011.06.036.

Braucher, R., Guillou, V., Bourlès, D.L., Arnold, M., Aumaître, G., Keddadouche, K., Nottoli, E., 2015. Preparation of ASTER in-house ^{10}Be/^{9}Be standard solutions. Nuclear Instruments and Methods in Phys. Res. Section B: Beam Interact. Mater. Atoms 361, 335–340. https://doi.org/10.1016/j.nimb.2015.06.012.

Brown, E.T., Edmond, J.M., Raisbeck, G.M., Yiou, F., Kurz, M.D., Brook, E.J., 1991. Examination of surface exposure ages of Antarctic moraines using in-situ produced ^{10}Be and ^{26}Al. Geochim. Cosmochim. Acta 55, 2269–2283. https://doi.org/10.1016/0016-7037(91)90103-C.

Chikán, G., Chikánné, Kókai A., 1984. A Nyugati-Mecsek földtani térképe [geological map of the Western Mecsek Mts.]. In: Magyar Állami Földtani Intézet (Geological Institute of Hungary), Budapest, vol. 1, 25000.

Chmeleff, J., von Blanckenburg, F., Kossert, K., Jakob, D., 2010. Determination of the ^{10}Be half-life by multicollector ICP-MS and liquid scintillation counting. Nuclear Instruments & Methods in Phys. Res., section B. Beam Interact. Mater. Atoms 268, 192–199. https://doi.org/10.1016/j.nimb.2009.09.012.

Codilean, A.T., Munack, H., Cohen, T.J., Saktura, W.M., Gray, A., Mudd, S.M., 2018. OCTOPUS: an open cosmogenic isotope and luminescence database. Earth System Sci. Data 10 (4), 2123–2139. https://doi.org/10.5194/essd-10-2123-2018.

Codilean, A.T., Munack, H., Saktura, W.M., Cohen, T.J., Jacobs, Z., Ulm, S., Hesse, P.P., Heyman, P., Peters, K.J., Williams, A.N., Sakutram, R.B.K., Rui, X., Chsihiro-Denelly, K., Panta, A., 2022. OCTOPUS Database v. 2. Earth System Sci. Data 14, 3695–3713. https://doi.org/10.5194/essd-14-3695-2022.

Corbett, L.B., Bierman, P.R., Graly, J.A., Neumann, T.A., Rood, D.H., 2013. Constraining landscape history and glacial erosivity using paired cosmogenic nuclides in Upernavik, Northwest Greenland. Geol. Soc. Am. Bull. 125, 1539–1553. https://doi.org/10.1130/B30813.1.

Csillag, G., Sebe, K., Pazonyi, P., 2023. Tengelici Vörösagyag Formáció [Tengelic Red clay Fm.]. In: Babinszki, E., Piros, O., Csillag, G., Fodor, L., Gyalog, L., Zs, Kercsmár, Gy, Less, Lukács, R., Sebe, K., Selmeczi, I., Szepesi, J., Sztanó, O., szerk. (Eds.), Magyarország litosztratigráfiai egységeinek leírása II. Kainozoos képződmények [Cenozoic Lithostratigraphic Units of Hungary II. Cenozoic Formations]. Supervising Authority of Regulated Activities, Budapest, p. 137.

Dixon, J.L., von Blanckenburg, F., Stüwe, K., Christl, M., 2016. Glaciation's topographic control on Holocene erosion at the eastern edge of the Alps. Earth Surf. Dyn. 4 (4), 895–909. https://doi.org/10.5194/esurf-4-895-2016.

Ehlers, J., Gibbard, P.L., 2004. Quaternary Glaciations-Extent and Chronology: Part I: Europe. Elsevier (475p Supplementary data).

Fenton, C.R., Binnie, S.A., Dunai, T., Niedermann, S., 2022. The SPICE project: calibrated cosmogenic ^{26}Al production rates and cross-calibrated ^{26}Al/^{10}Be, ^{26}Al/^{14}C, and ^{26}Al/^{21}Ne ratios in quartz from the SP basalt flow, AZ, USA. Quat. Geochronol. 67, 101218. https://doi.org/10.1016/j.quageo.2021.101218.

Feurdean, A., Perşoiu, A., Tanţău, I., Stevens, T., Magyari, E.K., Onac, B.P., Marković, S., Andrić, M., Connor, S., S., Farcäş, Gałka, M., Gaudenyi, T., Hoek, W., Kolaczek, P., Kuneš, P., Lamentowicz, M., Marinova, E., Michczyńska, D.J., Perşoiu, I., Płociennik, M., Słowinski, Stancikaite, M., Sumegi, P., Svensson, A., T., Tămaş, Timar, A., Tonkov, S., Toth, M., Veski, S., Willis, K.J., Zernitskaya, V., 2014. Climate variability and associated vegetation response throughout central and Eastern Europe (CEE) between 60 and 8 ka. Quat. Sci. Rev. 106, 206–224. https://doi.org/10.1016/j.quascirev.2014.06.003.

Freeman, S., Bishop, P., Bryant, C., Cook, G., Dougans, D., Ertunc, T., Fallick, A., Ganeshram, R., Maden, C., Naysmith, P., Schnabel, C., Scott, M., Summerfield, M., Xu, S., 2007. The SUERC AMS laboratory after 3 years. Nuclear Instruments and Methods in Phys. Res. Sect. B: Beam Interact. with Mater. and Atoms 259 (1), 66–70. https://doi.org/10.1016/j.nimb.2007.01.312.

Fülöp, R.-H., Codilean, A.T., Wilcken, K.M., Cohen, T.J., Fink, D., Smith, A.M., Yang, B., Levchenko, V.A., Wacker, L., Marx, S.K., 2020. Million-year lag times in a postorogenic sediment conveyor. Sci. Adv. 6 (25), eaaz8845. https://doi.org/10.1126/sciadv.aaz8845.

Granger, D.E., Riebe, C.S., 2014. Cosmogenic nuclides in weathering and erosion. In: Treatise on Geochemistry, 2nd edition 7, pp. 406–436. https://doi.org/10.1016/b978-0-08-095975-7.00514-3.

Granger, D.E., Schaller, M., 2014. Cosmogenic nuclides and Erosion at the watershed scale. Elements 10, 369–373. https://doi.org/10.2113/gselements.10.5.369.

Granger, D.E., Kirchner, J.W., Finkel, R., 1996. Spatially averaged long-term erosion rates measured from in situ-produced cosmogenic nuclides in alluvial sediments: J. Of. Geology 104, 3, 249–257. https://doi.org/10.1086/629823.

Gyalog, L., Síkhegyi, F. (Eds.), 2005. Magyarország földtani térképe, M=vol. 1:100 000 (Geological map of Hungary, 1:100 000). Magyar Állami Földtani Intézet (Geological Institute of Hungary), Budapest.

Haase, D., Fink, J., Haase, G., Ruske, R., Pécsi, M., Richter, H., Altermann, M., Jäger, K.-D., 2007. Loess in Europe - its spatial distribution based on a European loess map,

scale 1:2,500,000. Quat. Sci. Rev. 26, 1301–1312. https://doi.org/10.1016/j.quascirev.2007.02.003.
Halsted, C.T., Bierman, P.R., Codilean, A.T., Corbett, L.B., Caffee, M.W., 2025. Global analysis of in situ cosmogenic ^{26}Al and ^{10}Be and inferred erosion rate ratios in modern fluvial sediments indicates widespread sediment storage and burial during transport. Geochronol 7 (3), 213–228. https://doi.org/10.5194/gchron-7-213-2025.
Heisinger, B., Lal, D., Jull, A.J.T., Kubik, P., Ivy-Ochs, S., Neumaier, S., Knie, K., Lazarev, V., Nolte, E., 2002. Production of selected cosmogenic radionuclides by muons: 1. Fast muons. Earth Planet. Sci. Lett. 200 (3–4), 345–355. https://doi.org/10.1016/S0012-821X(02)00640-4.
Heisinger, B., Lal, D., Jull, A.J.T., Kubik, P., Ivy-Ochs, S., Knie, K., Nolte, E., 2002b. Production of selected cosmogenic radionuclides by muons: 2. Capture of negative muons. Earth Planet. Sci. Lett. 200 (3–4), 357–369. https://doi.org/10.1016/S0012-821X(02)00641-6.
Hetzel, R., Rother, H., Wolff, R., Hölzer, K., 2024. Millennial-scale erosion rates in the Harz Mountains (Germany) from cosmogenic ^{10}Be: implications for landscape evolution of basement highs in Central Europe. E&G Quat. Sci. J. 73 (2), 161–178.
Hippe, K., Kober, F., Zeilinger, G., Ivy-Ochs, S., Maden, C., Wacker, L., Kubik, P.W., Wieler, R., 2012. Quantifying denudation rates and sediment storage on the eastern Altiplano, Bolivia, using cosmogenic ^{10}Be, ^{26}Al, and in situ 14C. Geomorphology 179, 58–70. https://doi.org/10.1016/j.geomorph.2012.07.031.
Horváth, E., Bradák, B., 2014. Sárga föld, lősz, lösz: short historical overview of loess research and lithostratigraphy in Hungary. Quat. Int. 319, 1–10. https://doi.org/10.1016/j.quaint.2013.10.066.
Jautzy, T., Rixhon, G., Braucher, R., Delunel, R., Valla, P.G., Schmitt, L., Team, Aster, 2024. Cosmogenic (un-) steadiness revealed by paired-nuclide catchment-wide denudation rates in the formerly half-glaciated Vosges Mountains (NE France). Earth and Planet. Sci. Lett, 625, 118490. Aster Team. 2024.
Knudsen, M.F., Egholm, D.L., 2018. Constraining quaternary ice covers and erosion rates using cosmogenic ^{26}Al/^{10}Be nuclide concentrations. Quat. Sci. Rev. 181, 65–75. https://doi.org/10.1016/j.quascirev.2017.12.012.
Knudsen, M.F., Egholm, D.L., Jacobsen, B.H., Larsen, N.K., Jansen, J.D., Andersen, J.L., Linge, H.C., 2015. A multi-nuclide approach to constrain landscape evolution and past erosion rates in previously glaciated terrains. Quat. Geochronol. 30, 100–113. https://doi.org/10.1016/j.quageo.2015.08.004.
Kohl, C.P., Nishiizumi, K., 1992. Chemical isolation of quartz for measurement of in situ-produced cosmogenic nuclides. Geochim. Cosmochim. Acta 56, 3583–3587. https://doi.org/10.1016/0016-7037(92)90401-4.
Koloszár, L., Marsi, I., 2010. The thickest and most complete loess sequence in the Carpathian Basin: the borehole Udvari-2A. Cent. Eur. J. Geosci. 2 (2), 165–174. https://doi.org/10.2478/v10085-010-0004-9.
Korschinek, G., Bergmaier, A., Faestermann, T., Gerstmann, U.C., Knie, K., Rugel, G., Wallner, A., Dillmann, I., Dollinger, G., von Gostomski Ch., Lierse, Kossert, K., Maiti, M., Poutivtsev, M., Remmert, A., 2010. A new value for the half-life of ^{10}Be by heavy-ion elastic recoil detection and liquid scintillation counting. Nuclear Instruments & Methods in Phys. Res., Sect. B. Beam Interact. with Mater. and Atoms 268, 187–191. https://doi.org/10.1016/j.nimb.2009.09.020.
Kottek, M., Grieser, J., Beck, C., Rudolf, B., Rubel, F., 2006. World map of the Köppen-Geiger climate classification updated. Meteorol. Z. 15, 259–263. https://doi.org/10.1127/0941-2948/2006/0130.
Kovács, J., Fábián, S.Á., Varga, G., Újvári, G., Varga, G., Dezső, J., 2011. Plio-Pleistocene red clay deposits in the Pannonian basin: a review. Quat. Int. 240 (1–2), 35–43. https://doi.org/10.1016/j.quaint.2010.12.013.
Kovács, L., 2004. Research plan for phase 1 of the medium-term program for the qualification of the Boda Aleurolite Formation (BAF) (2004–2006). Manuscript, MECSEKÉRC Zrt. Archives, Pécs, p. 636 (in Hungarian).
Kukla, G., Cílek, V., 1996. Plio-Pleistocene megacycles: record of climate and tectonics. Palaeogeogr. Palaeoclimatol. Palaeoecol. 120, 171–194. https://doi.org/10.1016/0031-0182(95)00040-2.
Lal, D., 1991. Cosmic ray labeling of erosion surfaces; in situ nuclide production rates and erosion models: earth and planet. Sci. Lett. 104 (2–4), 424–439. https://doi.org/10.1016/0012-821X(91)90220-C.
Lehmkuhl, F., Nett, J.J., Pötter, S., Schulte, P., Sprafke, T., Jary, Z., Antoine, P., Wacha, L., Wolf, D., Zerboni, A., Hošek, J., Marković, S.B., Obreht, I., Sümegi, P., Veres, D., Zeeden, C., Boemke, B., Schaubert, V., Viehweger, J., Hambach, U., 2021. Loess landscapes of Europe–Mapping, geomorphology, and zonal differentiation. Earth Sci. Rev. 215, 103496. https://doi.org/10.1016/j.earscirev.2020.103496.
Lisiecki, L.E., Raymo, M.E., 2005. A Pliocene-Pleistocene stack of 57 globally distributed benthic δ^{18}O records. Paleoceanography 20, PA1003. https://doi.org/10.1029/2004PA001071.
Ludwig, P., Gavrilov, M.B., Markovic, S.B., Újvári, G., Lehmkuhl, F., 2021. Simulated regional dust cycle in the Carpathian Basin and the Adriatic Sea region during the last glacial maximum. Quat. Int. 581, 114–127. https://doi.org/10.18154/RWTH-2022-04520.
Magyar, I., Geary, D.H., Müller, P., 1999. Palaeogeographic evolution of the late Miocene Lake Pannon in Central Europe. Palaeogeogr. Palaeoclimatol. Palaeoecol. 147, 151–167. https://doi.org/10.1016/S0031-0182(98)00155-2.
Marković, S.B., Hambach, U., Stevens, T., Kukla, G.J., Heller, F., McCoy, W.D., Oches, E. A., Buggle, B., Zöller, L., 2011. The last million years recorded at the Stari Slankamen (northern Serbia) loess-palaeosol sequence: revised chronostratigraphy and long-term environmental trends. Quat. Sci. Rev. 30, 1142–1154. https://doi.org/10.1016/j.quascirev.2011.02.004.
Marković, S.B., Stevens, T., Kukla, G.J., Hambach, U., Fitzsimmons, K.E., Gibbard, P., Buggle, B., Zech, M., Guo, Z., Hao, Q., Wu, H., O'Hara-Dhand, K., Smalley, I.J., Újvári, G., Sümegi, P., Timar-Gabor, A., Veres, D., Sirocko, F., Vasiljević, D.A., Jary, Z., Svensson, A.M., Jović, V., Lehmkuhl, F., Kovács, J.I., Svirčev, Z., 2015. Danube loess stratigraphy—towards a pan-European loess stratigraphic model. Earth Sci. Rev. 148, 228–258. https://doi.org/10.1016/j.earscirev.2015.06.005.
Mehra, O.P., Jackson, M.L., 1960. Iron oxide removal from soils and clays by a dithionite-citrate system buffered with sodium bicarbonate. Clay Clay Miner. 7, 317–327. https://doi.org/10.1016/B978-0-08-009235-5.50026-7.
Merchel, S., Bremser, W., 2004. First international ^{26}Al interlaboratory comparison–part I. Nucl. Instrum. Meth. B. 223, 393–400. https://doi.org/10.1016/j.nimb.2004.04.076.
Merchel, S., Herpers, U., 1999. An update on radiochemical separation techniques for the determination of long-lived radionuclides via accelerator mass spectrometry. Radiochim. Acta 84, 215–219. https://doi.org/10.1524/ract.1999.84.4.215.
Merchel, S., Gärtner, A., Beutner, S., Bookhagen, B., Chabilan, A., 2019. Attempts to understand potential deficiencies in chemical procedures for AMS: cleaning and dissolving quartz for ^{10}Be and ^{26}Al analysis. Nucl. Instrum. Meth. B. 455, 293–299. https://doi.org/10.1016/J.NIMB.2019.05.005.
Mersich, I., Práger, T., Ambrózy, P., Hunkár, M., Dunkel, Z. (Eds.), 2001. Climate Atlas of Hungary (in Hungarian). Hungarian Meteorological Service, Budapest, p. 107.
Meyer, H., Hetzel, R., Strauss, H., 2010a. Erosion rates on different timescales derived from cosmogenic ^{10}Be and river loads: implications for landscape evolution in the Rhenish massif. Germany. Int. J. of Earth Sci. 99 (2), 395–412. https://doi.org/10.1007/s00531-008-0388-y.
Meyer, H., Hetzel, R., Fügenschuh, B., Strauss, H., 2010b. Determining the growth rate of topographic relief using in situ-produced ^{10}Be: a case study in the Black Forest. Germany. Earth and Planet. Sci. Lett 290 (3–4), 391–402. https://doi.org/10.1016/j.epsl.2009.12.034.
Nishiizumi, K., 2004. Preparation of Al-26 AMS standards. Nuclear Instruments & Methods in Phys. Res. Sect. B 223-24, 388–392. https://doi.org/10.1016/j.nimb.2004.04.075.
Nishiizumi, K., Lal, D., Klein, J., Middleton, R., Arnold, J.R., 1986. Production of ^{10}Be and 26Al by cosmic rays in terrestrial quartz in situ and implications for erosion rates. Nature 319 (6049), 134–136. https://doi.org/10.1038/319134a0.
Nishiizumi, K., Imamura, M., Caffee, M.W., Southon, J.R., Finkel, R.C., McAninch, J., 2007. Absolute calibration of Be-10 AMS standards. Nuclear Instruments & Methods in Phys. Res. Sect. B 258, 403–413. https://doi.org/10.1016/j.nimb.2007.01.297.
Nørgaard, J., Jansen, J.D., Neuhuber, S., Ruszkiczay-Rüdiger, Z., Knudsen, M.F., 2023. P–PINI. 2023. A cosmogenic nuclide burial dating method for landscapes undergoing non-steady erosion. Quat. Geochronol. 74, 101420. https://doi.org/10.1016/j.quageo.2022.101420.
Norton, K.P., von Blanckenburg, F., DiBiase, R., Schlunegger, F., Kubik, P.W., 2011. Cosmogenic ^{10}Be-derived denudation rates of the eastern and southern European Alps. Int. J. Earth Sci. 100 (5), 1163–1179. https://doi.org/10.1007/s00531-010-0626-y.
Nős, B., 2020. Needs of countries with longer timescale for deep geological repository implementation. EPJ Nuclear Sci. Technol. 6, 22. https://doi.org/10.1051/epjn/2019042.
Novothny, Á., Barta, G., Végh, T., Bradák, B., Surányi, G., Horváth, E., 2020. Correlation of drilling cores and the Paks brickyard key section at the area of Paks. Hungary. Quat. Int. 552, 50–61. https://doi.org/10.1016/j.quaint.2019.09.012.
Novothny, Á., Horváth, E., Újvári, G., 2023. Paksi Lösz Formáció [Paks Loess Formation]. In: Babinszki, E., Piros, O., Csillag, G., Fodor, L., Gyalog, L., Zs, Kercsmár, Gy, Less, Lukács, R., Sebe, K., Selmeczi, I., Szepesi, J., Sztanó, O., szerk. (Eds.), Magyarország litosztratigráfiai egységeinek leírása II. Kainozoos képződmények [Cenozoic Lithostratigraphic Units of Hungary II. Cenozoic Formations]. Supervising Authority of Regulated Activities, Budapest, pp. 158–160.
Obreht, I., Zeeden, C., Hambach, U., Veres, D., Marković, S.B., Lehmkuhl, F., 2019. A critical reevaluation of palaeoclimate proxy records from loess in the Carpathian Basin. Earth Sci. Rev. 190, 498–520. https://doi.org/10.1016/j.earscirev.2019.01.020.
Olivetti, V., Godard, V., Bellier, O., Team, Aster, 2016. Cenozoic rejuvenation events of massif central topography (France): insights from cosmogenic denudation rates and river profiles. Earth Planet. Sci. Lett. 444, 179–191. https://doi.org/10.1016/j.epsl.2016.03.049.
Pazonyi, P., 2004. Mammalian ecosystem dynamics in the Carpathian Basin during the last 27,000 years. Palaeogeogr. Palaeoclimatol. Palaeoecol. 212 (3–4), 295–314.
Portenga, E.W., Bierman, P.R., 2011. Understanding earth's eroding surface with ^{10}Be. GSA Today 21, 8. https://doi.org/10.1130/G111A.1.
Robl, J.C., Dremel, F., Stüwe, K., Hergarten, S., von Hagke, C., Fabel, D., 2024. Old orogen–young topography: lithological contrasts controlling erosion and relief formation in the bohemian massif. EGUsphere 2024, 1–33. https://doi.org/10.5194/egusphere-2024-3256.
Rugel, G., Pavetich, S., Akhmadaliev, S., Enamorado Baez, S.M., Scharf, A., Ziegenrücker, R., Merchel, S., 2016. The first four years of the AMS-facility DREAMS: status and developments for more accurate radionuclide data. Nucl. Instrum. Meth. B. 370, 94–100. https://doi.org/10.1016/j.nimb.2016.01.012.
Ruszkiczay-Rüdiger, Z., Braucher, R., Csillag, G., Fodor, L.I., Dunai, T.J., Bada, G., Müller, P., 2011. Dating Pleistocene aeolian landforms in Hungary, Central Europe, using in situ produced cosmogenic ^{10}Be. Quat. Geochronol. 6 (6), 515–529. https://doi.org/10.1016/j.quageo.2011.06.001.
Ruszkiczay-Rüdiger, Z., Neuhuber, S., Braucher, R., Lachner, J., Steier, P., Wieser, A., Braun, M., 2021. Comparison and performance of two cosmogenic nuclide sample preparation procedures of in situ produced ^{10}Be and ^{26}Al. J. Radioanal. Nucl. Chem. 329 (3), 1523–1536. https://doi.org/10.1007/s10967-021-07916-4.
Ruszkiczay-Rüdiger, Zs, Kern, Z., 2016. Permafrost or seasonal frost? - a review of paleoclimate proxies of the last glacial cycle in the east central European lowlands. Quat. Int. 415, 241–252. https://doi.org/10.1016/j.quaint.2015.07.027.

Schaller, M., von Blanckenburg, F., Hovius, N., Kubik, P.W., 2001. Large-scale erosion rates from in situ-produced cosmogenic nuclides in European river sediments: Earth and Planet. Sci. Lett. 188, 441–458. https://doi.org/10.1016/S0012-821X(01)00320-X.

Schaller, M., Ehlers, T.A., Stor, T., Torrent, J., Lobato, L., Christl, M., Vockenhuber, C., 2016. Spatial and temporal variations in denudation rates derived from cosmogenic nuclides in four European fluvial terrace sequences. Geomorphology 274, 180–192. https://doi.org/10.1016/j.geomorph.2016.08.018.

Schaller, M., Peifer, D., Neely, A.B., Bernard, T., Glotzbach, C., Beer, A.R., Ehlers, T.A., 2025. Spatiotemporal denudation rates of the Swabian Alb escarpment (Southwest Germany) dominated by base-level lowering and lithology. Earth Surf. Dyn. 13, 571–591. https://doi.org/10.5194/esurf-13-571-2025.

Sebe, K., Konrád, Gy, 2013. On the position and age of the highest-lying Lake Pannon deposits in the Mecsek Mts (SW Hungary). Földtani Közlöny 143/1, 67–72, in Hungarian, with English abstract. https://ojs.mtak.hu/index.php/foldtanikozlony/article/view/2318.

Sebe, K., Csillag, G., Konrád, G., 2008. The role of neotectonics in fluvial landscape development in the Western Mecsek Mountains and related foreland basins (SE Transdanubia, Hungary). Geomorphology 102 (1), 55–67.

Sebe, K., Csillag, G., Ruszkiczay-Rüdiger, Zs, Fodor, L., Thamó-Bozsó, E., Müller, P., Braucher, R., 2011. Wind erosion under cold climate: a fossil periglacial megayardang system in Central Europe (Western Pannonian Basin, Hungary). Geomorphology 134, 470–482. https://doi.org/10.1016/j.geomorph.2007.05.018.

Sebe, K., Józsa, S., Lukács, R., Surányi, G., Harangi, S., Novothny, Á., 2025. The preservation potential of loess in low-elevation mountains (Mecsek Mountains, Hungary). Quat. Res. 1-15. https://doi.org/10.1017/qua.2024.53.

Small, E.E., Anderson, R.S., Repka, J.L., Finkel, R., 1997. Erosion rates of alpine bedrock summit surfaces deduced from in situ ^{10}Be and ^{26}Al: Earth and Planet. Sci. Lett. 150 (3–4), 413–425. https://doi.org/10.1016/S0012-821X(97)00092-7.

Stone, J.O., 2000. Air pressure and cosmogenic isotope production. J. Geophys. Res. 105, 23753. https://doi.org/10.1029/2000JB900181.

Stroeven, A.P., Fabel, D., Hättestrand, C., Harbor, J., 2002. A relict landscape in the Centre of Fennoscandian glaciation: cosmogenic radionuclide evidence of tors preserved through multiple glacial cycles. Geomorphology 44 (1–2), 145–154. https://doi.org/10.1016/S0169-555X(01)00150-7.

Strunk, A., Knudsen, M.F., Egholm, D.L., Jansen, J.D., Levy, L.B., Jacobsen, B.H., Larsen, N.K., 2017. One million years of glaciation and denudation history in West Greenland. Nature Comm. 8 (1), 14199. https://doi.org/10.1038/ncomms14199.

Sümegi, P., Magyari, E., Dániel, P., Molnár, M., Törőcsik, T., 2013. Responses of terrestrial ecosystems to Dansgaard–Oeshger cycles and Heinrich-events: a 28,000-year record of environmental changes from SE Hungary. Quat. Int. 293, 34–50. https://doi.org/10.1016/j.quaint.2012.07.032.

Sümegi, P., Gulyás, S., Molnár, D., Sümegi, B.P., Almond, P.C., Vandenberghe, J., Zhou, L., Pál-Molnár, E., Törőcsik, T., Hao, Q., Smalley, I., Molnár, M., Marsi, I., 2018. New chronology of the best developed loess/paleosol sequence of Hungary capturing the past 1.1 ma: implications for correlation and proposed pan-Eurasian stratigraphic schemes. Quat. Sci. Rev. 191, 144–166. https://doi.org/10.1016/j.quascirev.2018.04.012.

Sümegi, P., Gulyás, S., Molnár, D., Sümegi, B.P., Törőcsik, T., Almond, P.C., Smalley, I., Galovic, L., Pál-Molnár, E., 2019. Periodicities of paleoclimate variations in the first high-resolution nonorbitally tuned grain size record of the past 1 ma from SW Hungary and regional, global correlations. Aeolian Res. 40, 74–90. https://doi.org/10.1016/j.aeolia.2019.07.002.

Thiel, C., Horváth, E., Frechen, M., 2014. Revisiting the loess/palaeosol sequence in Paks, Hungary: a post-IR IRSL based chronology for the 'younger loess series'. Quat. Int. 319, 88–98. https://doi.org/10.1016/j.quaint.2013.05.045.

Újvári, G., Molnár, M., Novothny, Á., Páll-Gergely, B., Kovács, J., Várhegyi, A., 2014a. AMS 14C and OSL/IRSL dating of the Dunaszekcső loess sequence (Hungary): chronology for 20 to 150 ka and implications for establishing reliable age–depth models for the last 40 ka. Quat. Sci. Rev. 106, 140–154. https://doi.org/10.1016/j.quascirev.2014.06.009.

Újvári, G., Varga, A., Raucsik, B., Kovács, J., 2014b. The Paks loess-paleosol sequence: a record of chemical weathering and provenance for the last 800ka in the mid-Carpathian Basin. Quat. Int. 319, 22–37. https://doi.org/10.1016/j.quaint.2012.04.004.

Újvári, G., Molnár, M., Páll-Gergely, B., 2016. Charcoal and mollusc shell 14C-dating of the Dunaszekcső loess record. Hungary. Quat. Geochronol. 35, 43–53. https://doi.org/10.1016/j.quageo.2016.05.005.

Vermeesch, P., 2007. CosmoCalc: an excel add-in for cosmogenic nuclide calculations. Geochem. Geophys. Geosyst. 8. https://doi.org/10.1029/2006GC001530Q08003.

Wittmann, H. Von, Blanckenburg, F., 2016. The geological significance of cosmogenic nuclides in large lowland river basins. Earth Sci. Rev. 159, 118–141. https://doi.org/10.1016/j.earscirev.2016.06.001.

Walcott-George, C.K., Balter-Kennedy, A., Briner, J.P., Schaefer, J.M., Young, N.E., 2025. Glacial erosion and history of Inglefield land, northwestern Greenland. Cryosphere 19 (6), 2067–2086. https://doi.org/10.5194/egusphere-2024-2983.

Wittmann, H., von Blanckenburg, F., Maurice, L., Guyot, J.-L., Kubik, P., 2011. Recycling of Amazon floodplain sediment quantified by cosmogenic Al-26 and be-10. Geology 39 (5), 467–470. https://doi.org/10.1130/G31829.1.

Xu, S., Freeman, S.P.H.T., Sanderson, D., Shanks, R.P., Wilcken, K.M., 2013. Cl can interfere with Al3+ AMS but B need not matter to be measurement. Nuclear Instruments & Methods in Phys. Research Sect. B-Beam Interact. Mater. Atoms 294, 403–405.

Xu, S., Freeman, S.P.H.T., Rood, D.H., Shanks, R.P., 2014. Al-26 interferences in accelerator mass spectrometry measurements. Nuclear Instruments & Methods in Phys. Research Sect. B-Beam Interact. Ater. Atoms 333, 42–45. https://doi.org/10.1016/j.nimb.2012.01.045.

Xu, S., Freeman, S.P.H.T., Rood, D.H., Shanks, R.P., 2015. Decadal ^{10}Be, ^{26}Al and ^{36}Cl QA measurements on the SUERC 5MV accelerator mass spectrometer. Nuclear Instruments and Methods in Phys. Res. Sect. B: Beam Interact. Mater. Atoms 361, 39–42. https://doi.org/10.1016/j.nimb.2015.03.064.

Young, N.E., Lesnek, A.J., Cuzzone, J.K., Briner, J.P., Badgeley, J.A., Balter-Kennedy, A., Graham, B.L., Cluett, A., Lamp, J.L., Schwartz, R., Tuna, T., Bard, E., Caffee, M.W., Zimmerman, S.R.H., Schaefer, J.M., 2021. In situ cosmogenic ^{10}Be–^{14}C–^{26}Al measurements from recently deglaciated bedrock as a new tool to decipher changes in Greenland ice sheet size. Clim. Past 17 (1), 419–450. https://doi.org/10.5194/cp-17-419-2021.